Engineering xxx (xxxx) xxx

Contents lists available at ScienceDirect

Engineering

journal homepage: www.elsevier.com/locate/eng

Research
Medical Engineering—Article

Bazi Bushen Capsule Rescues Menopausal Obesity–Induced Cognitive Impairment by Restoring AhR–*miR-23a*-Dependent Mitochondrial Bioenergetics

Xiaobin An [a,#], Wentao Xu [a,#], Haining Chen [a,#], Mingyou Zhang [a], Xiaojing Zhong [a], Jing Liu [a], Haihui Chen [a], Xinyue Zhao [a], Yan Wu [a], Jing Li [e], Jinan Yang [a], Meijie Chen [a], Lu Zeng [a], Jing Ma [a], Xuqiao Wang [a], Hongrong Li [c,d], Yanpeng Xue [a], Qin Wang [a], Dongyang Wang [a], Guitian Cong [a], Yunlong Hou [c,d], Zhenhua Jia [b,c,*], Jing Ai [a,*]

[a] *Department of Pharmacology & State Key Laboratory of Frigid Zone Cardiovascular Diseases, College of Pharmacy, Harbin Medical University, Harbin 150081, China*
[b] *Hebei Yiling Hospital, High-level TCM Key Disciplines of National Administration of Traditional Chinese Medicine—Luobing Theory, Shijiazhuang 050091, China*
[c] *National Key Laboratory for Innovation and Transformation of Luobing Theory, Shijiazhuang 050035, China*
[d] *New Drug Evaluation Center, Shijiazhuang Yiling Pharmaceutical Co., Ltd., Shijiazhuang 050035, China*
[e] *Department of Pathology and Electron Microscopic Center, Harbin Medical University, Harbin 150081, China*

ARTICLE INFO

Article history:
Received 22 April 2025
Revised 2 April 2026
Accepted 6 May 2026
Available online xxxx

Keywords:
Bazi Bushen capsule
Menopausal obesity
AhR–*miR-23a* axis
Mitochondrial dysfunction
Cognitive impairment

ABSTRACT

Postmenopausal women with obesity are at a significantly elevated risk of cognitive impairment. There is therefore an urgent need to uncover the underlying mechanisms of this impairment and develop effective therapeutic strategies. In this study, we demonstrated that treatment with the traditional Chinese herbal formulation Bazi Bushen capsule (BZBS; 1.4 and 2.8 $g\cdot kg^{-1}\cdot d^{-1}$) significantly alleviated cognitive deficits and restored hippocampal theta rhythm power and frequency in ovariectomized (OVX) high-fat diet-fed (OXHF) mice. Furthermore, we showed that BZBS improved mitochondrial function in the hippocampus, as evidenced by mitochondrial crista structure restoration, decreased reactive oxygen species (ROS) accumulation, and reduced adenosine triphosphate (ATP) depletion. By integrating bioinformatic, molecular, and neurophysiological methods, we found that BZBS inhibited the aryl hydrocarbon receptor (AhR)–*miR-23a* axis, which reactivated both the nicotinamide phosphoribosyltransferase (NAMPT)–nicotinamide adenine dinucleotide (NAD^+)–sirtuin 1 (SIRT1) and proliferator-activated receptor gamma coactivator 1 alpha (PGC-1α)–SIRT3 pathways, thus restoring mitochondrial function and increasing ATP levels. This study mechanistically validated the Qi-replenishing bioactivity of BZBS, which aligned with its therapeutic mechanism as informed by traditional Chinese medicine theory. Our findings identified BZBS as a promising therapeutic candidate for alleviating cognitive decline induced by menopausal obesity. Moreover, by elucidating the mechanisms of BZBS at the molecular level, we established a crucial foundation for the clinical use of this Chinese herbal medicine.

1. Introduction

Postmenopausal women face a heightened risk of cognitive impairment, with estrogen depletion identified as a key contributing factor [1,2]. Compounding this endocrine vulnerability, longitudinal epidemiological evidence indicates that midlife obesity further increases the risk of later-life cognitive decline in women [3]. Chronic hypercaloric nutrition, particularly a high-fat diet (HFD), is a primary driver of obesity. Experimental models have corroborated the neurotoxic synergy of an HFD with estrogen deprivation, with ovariectomized (OVX) HFD-fed (OXHF) mice developing accelerated cognitive deterioration [4,5]. Given the accelerating global obesity pandemic [6], identifying the potential molecular mechanisms that underlie menopausal obesity-induced cognitive impairment and corresponding effective treatment

---

[*] Corresponding authors.

E-mail addresses: jzhjiazhenhua@163.com (Z. Jia), aijing@ems.hrbmu.edu.cn (J. Ai).

[#] These authors contributed equally to this work.

https://doi.org/10.1016/j.eng.2026.05.005

Please cite this article as: X. An, W. Xu, H. Chen et al., Bazi Bushen Capsule Rescues Menopausal Obesity–Induced Cognitive Impairment by Restoring AhR–*miR-23a*-Dependent Mitochondrial Bioenergetics, Engineering, https://doi.org/10.1016/j.eng.2026.05.005

options may greatly benefit the cognitive health of obese middle-aged women.

Traditional Chinese medicine (TCM) is a network-targeting therapeutic paradigm for managing chronic multisystem disorders. Bazi Bushen capsule (BZBS), a Chinese herbal compound approved by the National Medical Products Administration (NMPA) of the People's Republic of China (No. B20020585), is used clinically to treat fatigue and forgetfulness [7]. Animal studies showed that BZBS protected against altered testicular morphology and cognitive decline in *D*-gal- and $NaNO_2$-induced aging mice by upregulating sirtuin 6 (SIRT6) [8,9]. Moreover, BZBS alleviated atherosclerosis through G-protein coupled estrogen receptor 1 (GPER1)-dependent anti-apoptotic and anti-inflammatory effects in OVX/apolipoprotein E-deficient ($Apoe^{-/-}$) mice [10]. These anti-aging, anti-cognitive decline, and blood lipid-regulating effects position BZBS as a promising therapeutic candidate for treating obesity-exacerbated cognitive decline in estrogen-depleted women. However, the therapeutic potential of BZBS for treating the dual effects of chronic HFD exposure and hypoestrogenism and its underlying mechanisms are unclear.

Emerging evidence has revealed the dual regulatory role of the aryl hydrocarbon receptor (AhR) in metabolic and neurodegenerative pathologies. The obesity-associated adipokine kynurenine (Kyn) exacerbates metabolic dysfunction by hyperactivating AhR [11]. Interestingly, AhR is sensitive to estrogen depletion [12]. Our previous study revealed a critical neuropathological association: in both aged and 5-month-old female OVX estrogen-deficient mouse models, elevated accumulation of intranuclear AhR in the hippocampal formation mechanistically drove memory impairment [13]. However, how AhR regulates cognitive decline in HFD-fed estrogen-deficient mice and the role of BZBS are unknown.

According to the *Huangdi Neijing* (*Yellow Emperor's Canon of Internal Medicine*), Qi is a vital force sustaining life, and its deficiency is the fundamental driver of aging. A contemporary bioenergetic study revealed striking parallels between the traditional concept of Qi and function of mitochondria, the cellular powerhouse that governs energy metabolism [14]. Mitochondria-derived adenosine triphosphate (ATP) production is a quantifiable manifestation of Qi in biomedical terms, as it supports systemic homeostasis and critically influences aging trajectories. Notably, mitochondrial dysfunction, characterized by low ATP generation and oxidative stress, has emerged as a central pathophysiological driver of age-related neurodegeneration and cardiovascular disorders [15]. Intriguingly, AhR has been shown to be a critical disruptor of mitochondrial homeostasis, with AhR activation exacerbating lipid peroxidation and cellular senescence by suppressing SIRT1 and SIRT3 [16,17], thereby impairing ATP synthesis and the redox balance. The AhR/SIRT signaling axis may constitute a mechanistic nexus linking an HFD and estrogen deficiency-associated mitochondrial dysfunction with cognitive decline. On the basis of the theory of the *Yellow Emperor's Canon of Internal Medicine*, BZBS is formulated to maintain a balance of Qi, blood, Yin, and Yang in the five viscera, and therefore elucidating the role of BZBS in mitochondrial function and clarifying the relationship between BZBS and both AhR and SIRTs warrant further investigation.

In this study, we investigated whether menopausal obesity disrupts mitochondrial bioenergetics through the AhR–*miR-23a* axis and whether BZBS mitigates this process by restoring nicotinamide phosphoribosyltransferase (NAMPT)–nicotinamide adenine dinucleotide (NAD^+)–sirtuin 1 (SIRT1) and proliferator-activated receptor gamma coactivator 1 alpha (PGC-1α)–SIRT3 pathway activity. This study provides a mechanistic validation of the Qi-replenishing bioactivity of BZBS. By integrating bioinformatic, molecular, and neurophysiological methods to decode BZBS mechanisms at the molecular level, we established a foundational pathway by which Chinese herbal medicine may achieve global acceptance.

2. Materials and methods

2.1. Chemicals and reagents

BZBS powder, comprising 16 characterized Chinese herbal components (Table 1), was provided by Hebei Shijiazhuang Yiling Pharmaceutical Co., Ltd. (Lot 2104001; China).

A BZBS suspension was prepared by homogenizing the powder in 0.5% sodium carboxymethylcellulose (CMC-NA; Cat. No. 419281; Sigma-Aldrich, USA) through sequential magnetic stirring and ultrasonication steps for 60 min. The mixture was stored at 4 °C. Fresh suspensions were prepared weekly for all *in vivo* administrations to maintain the consistency and bioactivity of the formulation.

Lyophilized BZBS powder was prepared by solubilizing BZBS powder (1.0 g) in a 50% (v/v) dimethyl sulfoxide (DMSO) aqueous solution, followed by sequential vortex mixing (3000 $r \cdot min^{-1}$, 5 min) and ultrasonication (40 kHz, 45 min). The mixture was centrifuged at 3200 *g* for 10 min (4 °C) to remove insoluble particulates. The clarified supernatant was flash-frozen at −70 °C for at least 24 h and lyophilized in a Christ Alpha 2-4 LSCplus freeze dryer (−50 °C under 1 Pa vacuum). The lyophilized powder was chemically stable when stored at −20 °C for 24 months. This specific preparation was exclusively used for *in vitro* cell culture experiments.

Normal chow (Cat. No. H10010) and high-fat chow (Cat. No. H10060) were acquired from Beijing Huafukang Biotechnology Co., Ltd. (China). The compositions of the normal and high-fat chow are shown in Tables S1 and S2 in Appendix A. Adeno-associated virus (AAV)-pre-*miR-23a-3p* and AAV-AhR-nNLS/mNLS viral vectors were constructed and packaged by GenePharma (China).

Chlorogenic acid (CGA; Cat. No. HY-N0055), osthole (OST; Cat. No. HY-N0054), schisandrin A (Sch A; Cat. No. HY-N0693), schisandrin B (Sch B; Cat. No. HY-N0089), hyperoside (HYP; Cat. No. HY-N0452), imperatorin (IMP; Cat. No. HY-N0285), and Kyn (Cat. No. HY-104026) were purchased from MedChemExpress (MCE, China). These were all dissolved in DMSO to specific concentrations.

2.2. Human blood sample preparation

Plasma samples were collected from overweight or obese postmenopausal women (body mass index (BMI) ≥ 24.0 $kg \cdot m^{-2}$) who underwent community health examinations. Detailed protocol is provided in Section S1.1 in Appendix A.

2.3. Animals and drug treatment

Female C57BL/6 mice (8 weeks old, (20 ± 2) g) were procured from Liaoning Changsheng Biotechnology Co., Ltd. (China) and acclimatized under controlled environmental conditions ((23 ± 1) °C, 55% ± 5% humidity, 12 h/12 h light/dark cycle) with *ad libitum* access to autoclaved water and standard chow. Mice were randomly allocated to experimental groups using a computer-generated random number table that ensured balanced baseline body weights among the groups. The following groups were used for experiments: the sham control group fed normal chow and the OXHF group. A BZBS suspension in 0.5% (w/v) CMC-Na (vehicle) was administered daily via intragastric gavage (i.g.) for 60 consecutive days, and an equivalent volume of vehicle was administered to the control group. On the basis of previous studies [18], the dosages of BZBS were 0.7, 1.4, and 2.8 $g \cdot kg^{-1} \cdot d^{-1}$. Oral

Table 1
The drug composition and proportion of BZBS.

Component name	Component source	Weight (g)	Ratio (%)
Fructus Lycii	*Lycium barbarum* L.	3.14	16
Semen Cuscutae	*Cuscuta chinensis* Lam.	5.68	28
Schisandrae chinensis	*Schisandra chinensis* (Turcz.) Baill.	1.05	5
Fructus Cnidii	*Cnidium monnieri* (L.) Cusson	0.80	4
Fructus Rosae Laevigatae	*Rosa laevigata* Michx.	0.80	4
Fructus Rubi	*Rubus idaeus* L.	0.80	4
Semen Allii Tuberosi	*Allium tuberosum* Rottler ex Spreng.	0.80	4
Fructus toosendan	*Melia azedarach* L.	0.52	3
Epimedii Folium	*Epimedium brevicornu* Maxim.	1.59	8
Radix Morindae Officinalis	*Gynochthodes officinalis* F.C.How	0.80	4
Herba Cistanches	*Cistanche deserticola* Y.C. Ma	0.80	4
Radix Rehmanniae Recens	*Rehmannia glutinosa* (Gaertn.) DC.	1.05	5
Radix Cyathulae	*Cyathula officinalis* K.C.Kuan	0.80	4
Radix Ginseng	*Panax ginseng* C. A. Mey.	0.57	3
Cervi Cornu Pantotrichum	Young unossified hairy antler of male Cervus	0.36	2
Hippocampus	Hippocampus Kelloggi	0.48	2
Total	—	20.00	100

donepezil (DON, 1 mg•kg^{-1}; Cat. No. D6821; Sigma-Aldrich) was used as a positive control (Table S3 in Appendix A). All behavioral tests, tissue collection, and subsequent molecular analyses were conducted by investigators blinded to the group assignments. Behavioral assessments were conducted during week 8 postintervention. Mice were euthanized via cervical dislocation under deep anesthesia (pentobarbital, 50 mg•kg^{-1} intraperitoneally (i.p.)) 24 h after the final behavioral testing, and the hippocampi were rapidly dissected on ice-cooled plates for subsequent molecular analyses.

All experimental protocols were approved by the Institutional Animal Care and Use Committee of Harbin Medical University (approval No. IRB3000722) and the Chinese Association for Laboratory Animal Sciences (approval No. A5655-01), and were conducted in strict compliance with EU Directive 2010/63/EU and ARRIVE guidelines 2.0.

2.4. Ovariectomy experiment

OVX surgery was performed as previously described [13]. Details are provided in Section S1.2 in Appendix A.

2.5. Behavioral tests

All animals underwent systematic behavioral acclimation comprising 2 min daily handling sessions by investigators for two consecutive days and 30 min of environmental habituation in the testing arena prior to each experiment. A 24 h inter-test interval was strictly followed to mitigate carryover effects between assessments. Cognitive performance was evaluated using the Barnes maze (spatial memory) and novel object recognition (NOR) tests (episodic memory). Behavioral parameters were recorded by a XinRuan behavior analysis system (China).

The Barnes maze and NOR tests were performed as previously described [13]. Nesting behavior was evaluated following established ethological protocols [19] with minor adjustments. Detailed protocol is provided in Sections S1.3, S1.4, and S1.5 in Appendix A.

2.6. Transmission electron microscopy (TEM)

TEM was performed according to our previously published methods [20]. Detailed protocol is provided in Section S1.6 in Appendix A

2.7. Primary hippocampal neuron culture and treatment

Hippocampal tissue was aseptically dissected from postnatal day 0 Sprague–Dawley rat pups and enzymatically dissociated using 0.25% trypsin in a shaking water bath (37 °C, 60 r•mim^{-1}) for 15 min with gentle trituration every 5 min using fire-polished Pasteur pipettes. Enzymatic digestion was terminated by adding Dulbecco's modified eagle medium (DMEM; Cat. No. 11965092; Invitrogen, USA) supplemented with 10% heat-inactivated fetal bovine serum (Cat. No. 3022A; Umedium, China). The mixture was centrifuged (1000g, 5 min, 4 °C) and the pellet was resuspended in complete culture medium. The cell suspension was plated on poly-*D*-lysine-coated six-well plates at a density of 1×10^6 cells per well. After 4 h of incubation, the medium was replaced with serum-free neurobasal medium (Cat. No. 10888022; Gibco, USA) supplemented with 2% B27 (Cat. No. 17504044; Invitrogen), 0.5 mmol•L^{-1} *L*-glutamine, and 1% penicillin–streptomycin. Cultures were maintained at 37 °C in a 5% CO_2 humidified incubator, with half-medium changes every three days. The neurons were used 5–7 days after plating in all experiments.

Oligonucleotide synthesis was performed as previously reported [13]. Cultures were transfected with an *miR-23a* mimic, and parallel cultures were treated with 400 μg•mL^{-1} BZBS lyophilizate dissolved in neurobasal medium. After the transfected cells incubated at 37 °C for 6 h, the medium was replaced with fresh conditioned medium.

2.8. Construction of Ahr overexpression plasmids

The pcDNA3.1-3xFlag-C vector was used as the backbone to construct *Ahr* overexpression plasmids. Two types of plasmids were generated: one with an intact nuclear localization signal (NLS) and the other with a mutated NLS. The plasmid with the intact NLS was based on the full-length rat AhR complementary DNA (cDNA) according to National Center for Biotechnology Information (NCBI) RefSeq protein sequence NP_001295183.1 and contained the native NLS motifs 12–15 (RKRR) and 36–38 (KRH). The cDNA was amplified by PCR and cloned into the pcDNA3.1-3xFlag-C vector between the appropriate restriction enzyme sites. The NLS-mutated plasmid was generated using site-directed mutagenesis to replace the arginine residues at positions 12, 14, and 37 of *Ahr* with alanine residues, with the wild-type *Ahr* overexpression plasmid as the template. All constructed plasmids were verified by DNA sequencing to ensure that the fragment was properly inserted and the mutation sites were correct.

2.9. Dual-luciferase reporter assay

A dual-luciferase reporter assay was performed as previously reported [21]. HEK293T cells at ~50% confluence were co-transfected with a 20 nmol•L^{-1} *miR-23a* mimic (*miR-23a*), antisense oligonucleotide inhibitor (AMO-23a), or scrambled negative control (NC) small interfering RNA (siRNA), along with 0.5 μg of the psiCHECK-2-*Nampt* 3′ untranslated region (UTR) wild-type or mutant reporter plasmid expressing firefly luciferase and 1 μg of the empty vector (pcDNA3.1). Lipofectamine 2000 (Cat. No. 11668019; Invitrogen) at a 3:1 reagent-to-DNA ratio was used for transfection. Site-directed mutagenesis of the predicted *miR-23a* binding sites in the *Nampt* 3′ UTR was performed by overlap extension PCR with synthesized mutagenic primers (Sangon Biotech, China). All the constructs were sequence-verified by Sanger sequencing (TSINGKE Biotechnology, China). Forty-eight hours post-transfection, the cells were lysed with passive lysis buffer (1×; Cat. No. C8011; Promega, USA), and the luciferase activity was quantified using a GloMax Navigator luminometer (Promega) with sequential measurements of Renilla (50 μL of coelenterazine substrate) and firefly luciferase (50 μL of luciferase assay reagent II) signals. Relative luciferase activity was normalized to the Renilla/firefly luminescence ratio, with empty vector-transfected samples serving as baseline controls.

2.10. Quantitative real-time PCR (qRT-PCR)

qRT-PCR was performed as previously described [13]. Detailed protocol is provided in Section S1.7 in Appendix A.

2.11. Mitochondrial respiration measurements

Mitochondrial respiration was measured as previously reported [22]. Primary hippocampal neurons were isolated via trypsin digestion, centrifuged (1000g, 5 min), resuspended in DMEM, and plated at a density of 3×10^6–4×10^6 cells per well. Mitochondrial respiratory function was assessed using high-resolution respirometry (Oxygraph-2k; Oroboros Instruments, Austria) with the following sequential substrate-inhibitor titrations: ① Basal respiration was measured in assay buffer; ② oligomycin (1 μmol•L^{-1}; Cat. No. HY-N6782; MCE) was added to induce a non-phosphorylating (leak) state; ③ carbonyl cyanide 4-(trifluoromethoxy) phenylhydrazone (FCCP; 2 μmol•L^{-1}; Cat. No. HY-N6782; MCE) was titrated to uncouple the mitochondria and thus determine the maximum electron transport system capacity; and ④ rotenone (1 μmol•L^{-1}; complex I inhibitor; Cat. No. HY-B1756; MCE) and antimycin A (5 μmol•L^{-1}; complex III inhibitor; Cat. No. MS0070; Shanghai Maokang Biotechnology Co., Ltd., China) were added to inhibit residual oxygen consumption. Data were normalized to cell counts and analyzed using DatLab 7.4 software (Oroboros Instruments) to determine key parameters, including basal respiration, ATP-linked respiration, maximal respiratory capacity, and spare respiratory capacity.

2.12. Stereotaxic injection of AAV

A scrambled control sequence was injected as a NC. AAV was synthesized and packaged according to our previously reported study [13]. Detailed protocol is provided in Section S1.8 in Appendix A.

2.13. ATP determination

An ATP assay kit (Cat. No. S0026B; Beyotime Biotechnology, China) was used to determine ATP levels in both the cells and tissue. Detailed protocol is provided in Section S1.9 in Appendix A.

2.14. Glutathione (GSH) determination

A GSH assay kit (Cat. No. S00052; Beyotime Biotechnology) was used to measure GSH levels in the cells and tissue. Detailed protocol is provided in Section S1.10 in Appendix A.

2.15. Reactive oxygen species (ROS) determination

ROS levels were measured as previously described [18]. Detailed protocol is provided in Section S1.11 in Appendix A.

2.16. Total NAD$^+$ determination

An NAD$^+$ assay kit (Cat. No. S0175; Beyotime Biotechnology) was used to measure the total NAD$^+$ concentration in the cells and tissue. Detailed protocol is provided in Section S1.12 in Appendix A.

2.17. Western blot

Total protein was extracted from mouse hippocampi and cultured cells. Detailed protocol and detailed information of primary antibodies are provided in Section S1.13 and Table S4 in Appendix A.

2.18. Bioinformatic analysis

Bioactive phytochemicals in BZBS related to cognitive impairment-associated pathways were identified. A systems pharmacology method was used to characterize the bioactive constituents of BZBS potentially involved in cognitive impairment- and oxidative stress-related pathways. Targets of 14 BZBS phytochemicals (Table S5 in Appendix A) were predicted using SwissTargetPrediction (STP) [23], which were screened in the Traditional Chinese Medicine Systems Pharmacology Database (TCMSP) for Alzheimer's disease (AD) relevance [24]. Compound target disease networks were constructed in Cytoscape (v3.9.1) using the NetworkAnalyzer toolkit.

Functional enrichment profiling was performed by analyzing the Gene Ontology (GO) and Kyoto Encyclopedia of Genes and Genomes (KEGG) databased using the R "clusterProfiler" and "ggplot2" packages. ClueGO was used to reveal the GO pathway network.

Molecular docking was conducted to investigate the binding interactions between AhR and the four bioactive compounds in BZBS: CGA, OST, Sch A, and Sch B. The crystal structure of AhR was obtained from the AlphaFold protein structure database and the 3D structures of the four bioactive compounds were obtained from the NCBI PubChem database. Docking simulations were performed using AutoDock 1.5.7 with 3D conformers of the receptor and ligands. The lowest free energy docking poses were visualized and analyzed using PyMOL 2.5.0. Binding affinities ≤ −5.0 kcal•mol^{-1} were considered to indicate strong receptor–ligand interactions [25].

2.19. Local field potential (LFP) recording

LFPs were obtained as previously reported [4]. LFPs in the dorsal hippocampal CA1 region were recorded under anesthesia. Detailed protocol is provided in Section S1.14 in Appendix A.

2.20. Immunohistochemistry

Immunofluorescence staining was performed as previously reported [4]. Detailed protocol is provided in Section S1.15 in Appendix A.

2.21. Chromatin immunoprecipitation (ChIP) assay

A ChIP assay was performed as previously described [13]. Prior to performing the ChIP assay, the *miR-23a-3p* promoter sequence was retrieved from the University of California, Santa Cruz (UCSC) Genome Browser and input into the JASPAR database for predicting transcription factors. Thirty-two putative binding sites were predicted between AhR and the promoter sequence of *miR-23a-3p*. Samples were divided into three groups for the ChIP hippocampal tissue assay: the sham group, OXHF group, and BSBZ group. The assay was performed with an imprint ChIP assay kit (Cat. No. 26156; Thermo Fisher Scientific, USA) in accordance with the manufacturer's instructions. The PCR primers used in the assay were as follows: NC ChIP forward primer (F)1, 5'-GGAAGGACAGCATCATGCCG-3'; NC ChIP reverse primer (R)1, 5'-ATTATTCCCAGGCCCAAAGC-3'; *miR-23a-3p* F2, 5'-CCAGAAGAGGGAGTCAGATC-3'; *miR-23a-3p* R2, 5'-TGTCATGCACAAAGACCAGAC-3'; *miR-23a-3p* F3, 5'-GATAGCTGTGCTTGTCATGTAG-3'; *miR-23a-3p* R3, 5'-GAGAAGGTATTTAGCACCCAG-3'; *miR-23a-3p* F4, 5'-TGGAAGTAGAGGAGGGCTAG-3'; and *miR-23a-3p* R4, 5'-TAGCACCTAAAGAGAGAAAG-3'. These primers were designed to amplify fragments 260, 218, 324, and 241 bp in size, respectively, from selected genomic regions of *miR-23a-3p*. qRT PCR of the genomic regions containing the putative AhR-binding sites was performed on each sample in the three groups in triplicate. The cycling parameters were as follows: initial denaturation at 98 °C for 5 min; 35 cycles of denaturation at 98 °C for 30 s, annealing at 55 °C for 20 s, and extension at 68 °C for 20 s; and a final extension at 72 °C for 5 min. The relative occupancy of each immunoprecipitated factor at a locus was estimated by the comparative threshold method.

2.22. Cellular thermal shift assay (CETSA)

A CETSA was performed as previously described with modifications [26]. SH-SY5Y cells were treated with BZBS (400 $\mu g \cdot mL^{-1}$) and incubated at 37 °C for 6 h. The cells were then exposed to specific temperatures for 5 min at each temperature. Immediately afterward, the samples were snap-frozen in liquid nitrogen and subjected to three freeze–thaw cycles. Finally, the lysates were centrifuged at 12 000 $r \cdot min^{-1}$ for 10 min, and the supernatant was collected for Western blot analysis.

2.23. Statistical analysis

All quantitative data are presented as mean ± standard error of the mean (SEM). Data quantification and statistical analyses were performed blindly, with the analyst unaware of group identities during data processing. Between-group differences were analyzed by a two-tailed unpaired Student's *t*-test with Welch's correction for unequal variances. Comparisons among three or more groups were conducted using one-way analysis of variance (ANOVA) with post hoc multiple comparisons adjusted by Tukey's honestly significant difference test when omnibus *F*-values reached significance ($P < 0.05$). All statistical tests were implemented in GraphPad Prism 8.0 (GraphPad Software, USA), with graphical representations generated using the software's built-in data visualization toolkit.

3. Results

3.1. BZBS rescues cognitive deficits and hippocampal mitochondrial dysfunction in OXHF mice

To evaluate the therapeutic potential of BZBS for treating cognitive decline associated with menopausal obesity, we established an OXHF mouse model and treated the mice with BZBS (0.7, 1.4, or 2.8 $g \cdot kg^{-1} \cdot d^{-1}$) or DON (1 $mg \cdot kg^{-1} \cdot d^{-1}$) by gavage daily for eight weeks (Fig. 1(a)). Consistent with previous reports [10], BZBS significantly inhibited body weight gain and attenuated the increase in total cholesterol and triglyceride plasma levels of OXHF mice (Fig. S1 in Appendix A). We then performed the Barnes maze test to evaluate the spatial memory of the mice (Fig. 1(b)). The OXHF-treated mice showed significantly longer search distances than the sham-treated control mice (Fig. 1(c)) during the probe trial. Moreover, they exhibited extended latencies (Fig. 1(d)) and an increased number of errors (Fig. 1(e)). These differences were effectively ameliorated by treatment with BZBS at doses of 1.4 and 2.8 $g \cdot kg^{-1}$ (Figs. 1(c)–(e)); however, no effect was observed during the training period (Fig. S2 in Appendix A). We then investigated the means by which BZBS influenced the episodic memory of OXHF-treated mice using the NOR test. We found that when we replaced object B with the novel object C on the second day, there was a significant decrease in either the exploration time or the preference for the novel object C in OXHF mice compared with sham control mice, and this change was successfully reversed by BZBS (1.4 and 2.8 $g \cdot kg^{-1}$) (Figs. 1(f)–(i), Fig. S3 in Appendix A). Additionally, OXHF mice treated with BZBS (1.4 and 2.8 $g \cdot kg^{-1}$) had better nesting scores than OXHF mice without drug intervention (Figs. 1(j) and (k)). All the effects of BZBS were similar to those of DON (Figs. 1(b)–(k)). Notably, BZBS at a dose of 0.7 $g \cdot kg^{-1}$ did not reduce the cognitive deficits that occurred in OXHF mice, including reduced spatial memory, episodic memory, and nest building ability (Fig. 1). These results indicated that BZBS ameliorated cognitive impairment in OXHF mice, with an effective dose threshold of 1.4 $g \cdot kg^{-1} \cdot d^{-1}$.

Given the established link between mitochondrial dysfunction and neurodegenerative aging [27], we investigated whether BZBS-mediated cognitive protection involved mitochondrial rescue. TEM of the hippocampi of OXHF mice revealed severe mitochondrial damage as evidenced by swelling and loss of cristae (Fig. 2(a)). These changes were confirmed by increased ROS levels and reduced GSH and ATP levels in the hippocampi of OXHF mice compared with those in sham control mice (Figs. 2(b)–(e)). BZBS (1.4 and 2.8 $g \cdot kg^{-1}$) effectively reversed these changes (Figs. 2(b)–(e)). Notably, the effects of BZBS were similar to those of DON (Figs. 2(b)–(e)), which was previously reported to inhibit ROS generation [28]. Consistent with these *in vivo* cognitive data, BZBS at a dose of 0.7 $g \cdot kg^{-1}$ failed to achieve these protective effects on the hippocampal mitochondria of OXHF mice. These results suggest that the protective effects of BZBS on hippocampal mitochondria are related to the ability of BZBS to prevent decreased cognition in OXHF mice.

3.2. BZBS restores mitochondrial bioenergetics through the dual modulation of miR-23a-dependent pathways

The sirtuin (SIRT1–7) family comprises key proteins that regulate ATP and ROS formation [29]. However, it is not known whether the SIRT family participates in OXHF-induced mitochondrial dysfunction. A comprehensive profiling of hippocampal SIRT levels revealed that SIRT1 and SIRT3 were selectively downregulated in OXHF mice, whereas levels of other isoforms (SIRT2/4–7) remained unchanged (Fig. S4 in Appendix A). BZBS treatment (1.4 and 2.8 $g \cdot kg^{-1}$) restored the protein levels of both SIRT1 and SIRT3 to near physiological levels in the hippocampi of OXHF mice (Figs. 3(a) and (b)). Strikingly, although DON rescued levels of SIRT1 protein, it did not affect levels of SIRT3 (Figs. 3(a) and (b)). These data imply distinct mechanisms between the two therapeutics despite their comparable antioxidant and cognitive benefits.

SIRT3, a mitochondrial-localized deacetylase that is central to oxidative metabolism, is transcriptionally regulated by PGC-1α [30], which is a key regulator of mitochondrial biogenesis and redox homeostasis [31,32]. Our prior work established a mechanistic link between estrogen deficiency and mitochondrial dysfunction, in which OVX surgery induced cardiac PGC-1α deficiency through *miR-23*a-mediated posttranscriptional repression [33]. The regulatory microRNA *miR-23a* was shown to be elevated in the circulation of aging females [20]. Consistently, our analysis of

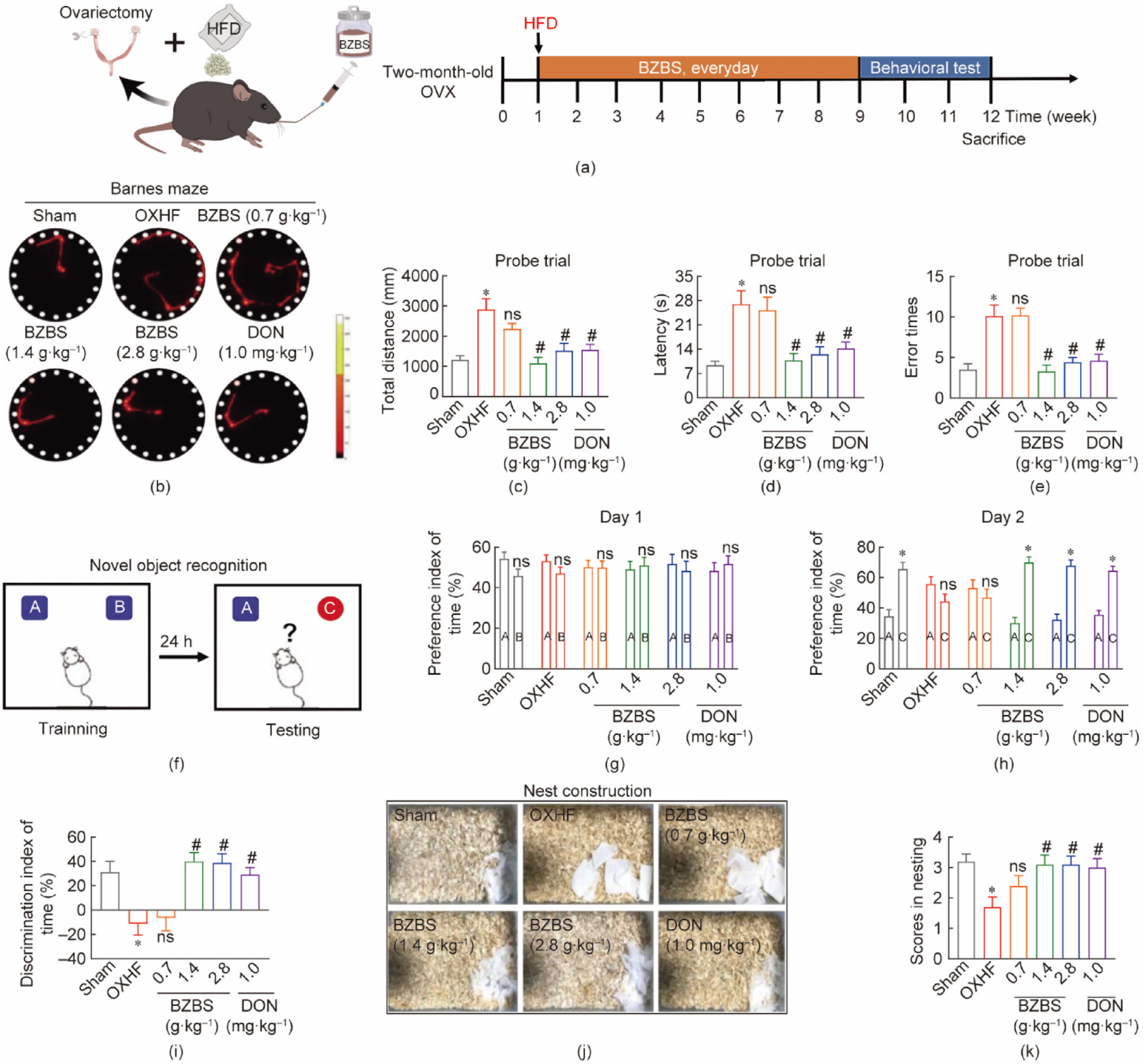

Fig. 1. BZBS improves cognitive deficits in OXHF mice. (a) Experimental timeline: OVX mice received daily oral BZBS for eight weeks. (b) Heatmap visualization of exploration patterns in the Barnes maze. (c–e) Cognitive performance metrics on day 9: BZBS-treated mice presented a reduced (c) total distance traveled, (d) shorter latency, and (e) fewer error times than OXHF controls when the target hole was located. (f) NOR test protocol. (g) Comparison of exploration times for familiar objects (A/B) across groups on day 1. (h, i) On day 2, BZBS intervention restored novel object preference, as evidenced by (h) increased exploration time for object C and (i) increased discrimination indices compared with those of OXHF mice. (j, k) Nest-building assessment: BZBS-treated mice achieved (k) significantly higher nest construction scores than their OXHF counterparts did, with (j) representative nest structures shown. $n = 10$ mice for each group. The data in all the graphs are presented as the mean ± SEM. One-way ANOVA or t-test, $^*P < 0.05$ vs the sham group, $^\#P < 0.05$ vs the OXHF group, ns: not significant.

human plasma samples showed that *miR-23a* levels were also increased in overweight and obese postmenopausal women and were negatively associated with Montreal Cognitive Assessment (MoCA) scores (Fig. S5 in Appendix A). These results suggest that *miR-23a* may be a systemic mediator in postmenopausal women and therefore a potential therapeutic target. Surprisingly, we found that the PGC-1α level in the hippocampus of OXHF mice was significantly lower than in the sham control mice (Fig. 3(c)), whereas the *miR-23a* expression was higher. These effects were reversed by BZBS treatment (1.4 and 2.8 g•kg^{-1}) (Fig. 3(d)). Neither BZBS (0.7 g•kg^{-1}) nor DON altered the level of PGC-1α or the expression of *miR-23a* (Figs. 3(c) and (d)). As predicted, *miR-23a* overexpression significantly inhibited the levels of both PGC-1α and SIRT3 *in vitro* (Figs. S6 in Appendix A). Similarly, BZBS effectively prevented the downregulation of both PGC-1α and SIRT3 induced by *miR-23a* overexpression (Figs. S6 in Appendix A). These findings established *miR-23a* as an upstream epigenetic regulator of the PGC-1α SIRT3 axis in OXHF-induced mitochondrial dysfunction.

However, an initial bioinformatic screening using established microRNA prediction platforms (TargetScan 8.0 and PicTar 4.0) failed to identify putative *miR-23a* binding sites within the 3′ UTRs of either SIRT3 or SIRT1 messenger RNA. The SIRT family consists of NAD$^+$-dependent protein deacetylases that are crucial regulators of cellular processes [34] and emerging evidence has suggested a positive correlation between NAD$^+$ availability and SIRT1 level, as NAD$^+$ depletion was shown to significantly downregulate SIRT1 expression [35]. Therefore, we quantitatively analyzed the NAD$^+$ concentration in the hippocampi of OXHF mice. As predicted, the

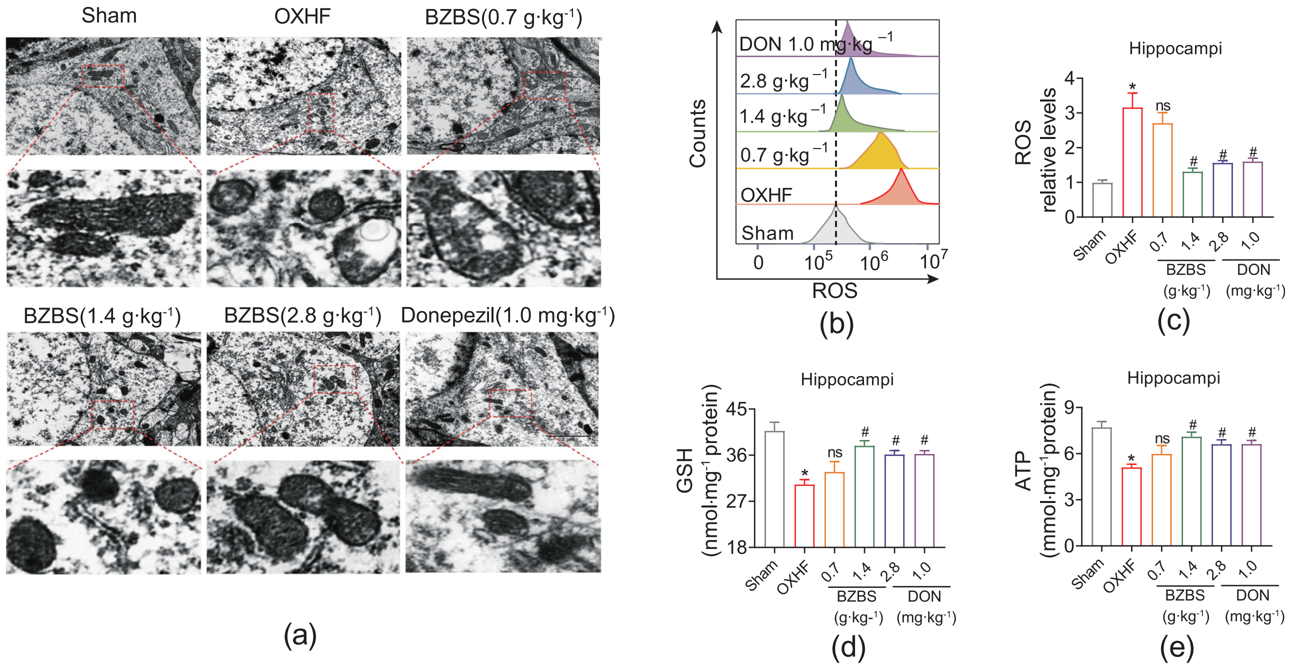

Fig. 2. BZBS mitigates hippocampal mitochondrial dysfunction in OXHF mice. (a) Ultrastructural analysis of hippocampal mitochondria in each group. Scan bar: 2 μm. $n = 4$ mice for each group. (b) Representative histograms of the mean fluorescence intensity (MFI) of ROS in the six groups and (c) quantification of the MFI of ROS in the six groups. (d, e) The levels of hippocampal (d) GSH and (e) ATP in all groups. $n = 6$ mice for each group. The data in all the graphs are presented as the mean ± SEM. One-way ANOVA, $^{*}P < 0.05$ vs the sham group, $^{\#}P < 0.05$ vs the OXHF group, ns: not significant.

NAD^+ concentration was significantly lower in the hippocampi of OXHF mice than in those of age-matched sham control mice (Fig. S7 in Appendix A). Surprisingly, these effects were reversed by BZBS (1.4 and 2.8 $g\cdot kg^{-1}$) but not by DON (Fig. 3(e)). To elucidate the mechanistic basis by which BZBS restored NAD^+ levels, we focused on the NAMPT-dependent salvage pathway, the predominant NAD^+ biosynthetic route in mammals [36]. This pathway includes sequential catalysis by NAMPT (converting nicotinamide (NAM) to nicotinamide mononucleotide (NMN)) and nicotinamide mononucleotide adenylyltransferase (NMNAT) isoforms (synthesizing NAD^+ from NMN) (Fig. 3(f)). Western blot analysis revealed that NAMPT levels were significantly reduced in OXHF mice (Fig. S8(a) in Appendix A); however, no observable changes were detected in NMNAT2 or NMNAT3 levels compared with age-matched sham control mice (Figs. S8(b) and (c) in Appendix A). Notably, BZBS treatment (1.4 and 2.8 $g\cdot kg^{-1}$) specifically rescued NAMPT levels in the hippocampi of OXHF mice; this effect was not detected with DON treatment (Fig. 3(g)).

To elucidate the molecular basis of NAMPT dysregulation and BZBS-mediated protection, we again conducted a bioinformatic screening using the microRNA prediction platforms TargetScan 8.0 and PicTar 4.0 and identified a conserved *miR-23a* binding motif within the 3′ UTR of the *Nampt* gene (Fig. 3(h)). Compared with the NC, functional validation based on dual-luciferase reporter assays in HEK293T cells demonstrated that transfection with *miR-23a* mimics markedly inhibited luciferase signals (Fig. 3(i)). However, the luciferase signals were diminished when the 3′ UTR of *Nampt* was mutated (Fig. 3(i)). Furthermore, we found that *miR-23a* overexpression significantly inhibited NAMPT, NAD^+, and SIRT1 levels (Fig. S9 in Appendix A). Importantly, BZBS (1.4 and 2.8 $g\cdot kg^{-1}$) effectively prevented these changes (Fig. S9). Furthermore, ROS levels decreased (Figs. 3(j) and (k)), GSH levels increased (Fig. 3(l)), and the oxygen consumption rate (OCR) increased in response to BZBS (Figs. 3(m)–(o)). These results suggest that, unlike DON, the protective effects of BZBS on mitochondrial function are mediated in part by the *miR-23a*–NAMPT–NAD^+–SIRT1 axis.

3.3. *miR-23a* contributes to the protection against cognitive decline exerted by BZBS in OXHF mice

To further investigate the role of *miR-23a* in BZBS-mediated cognitive preservation, we established a *miR-23a*-overexpressing mouse model by injecting AAV-pre-*miR-23a* bilaterally into the hippocampal CA1 regions of adult normal female mice. The mice were then administered BZBS (1.4 $g\cdot kg^{-1}$) via gavage for two months (Fig. 4(a)). The mice in the NC group underwent identical stereotaxic surgery and virus injection procedures as those of the experimental group but with a control virus that did not express *miR-23a*. As shown in Fig. 4(b), AAV-pre-*miR-23a* injection significantly upregulated *miR-23a* expression in the mouse hippocampi; this upregulation was inhibited by BZBS treatment. A Barnes maze test assessment (Figs. 4(c)–(f)) revealed that, compared with NC mice, mice injected with AAV-pre-*miR-23a* showed significantly increased search distances, prolonged latencies, and an increase in the number of errors when finding the target hole, all of which were ameliorated by BZBS treatment. Similarly, *miR-23a* overexpression also impaired episodic memory and nest building in mice, but these cognitive impairments were reversed by BZBS treatment (Figs. S10 and S11 in Appendix A). As anticipated, *miR-23a* overexpression in the hippocampi induced by AAV-pre-*miR-23a* injection significantly downregulated the protein level of NAMPT, reduced the content of NAD^+, and inhibited SIRT1 level, all of which were reversed by BZBS treatment (Figs. 4(g)–(i)). Concurrently, BZBS treatment also ameliorated the reduced levels of PGC-1α and SIRT3 in the hippocampi of mice caused by AAV-pre-*miR-23a* injection (Figs. 4(j) and (k)). Functionally, BZBS protected against increased ROS levels and reduced GSH and ATP levels induced by *miR-23a* overexpression (Fig. 4(l)–(o)). These results suggest that BZBS protects against cognitive decline induced by *miR-23a* overexpression.

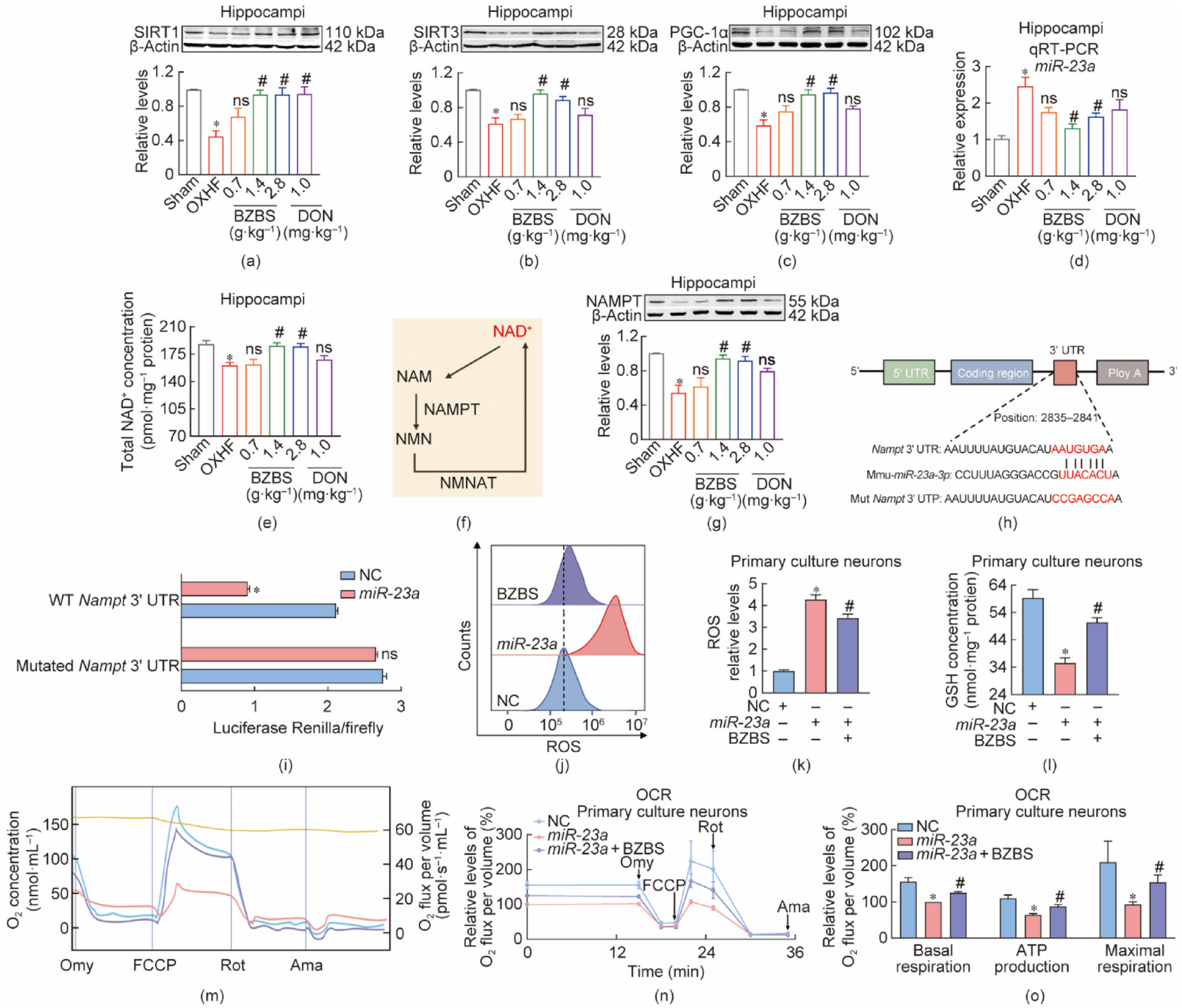

Fig. 3. BZBS restores redox homeostasis via the *miR-23a*-dependent regulation of the NAMPT–NAD$^+$–SIRT1 and PGC-1α–SIRT3 pathways. (a–c) OXHF mice presented a decrease in hippocampal (a) SIRT1, (b) SIRT3, and (c) PGC-1α levels, which was prevented by BZBS treatment. (d) BZBS treatment blocked the increase in hippocampal *miR-23a* in OXHF mice. (e) The levels of total NAD$^+$ in the hippocampi of the mice in each group. (f) NAD$^+$ biosynthetic pathways in mammals. NAMPT recycles NAM into NMN, which is then converted into NAD$^+$ via different NMNATs. (g) BZBS improved the level of NAMPT in the hippocampi of OXHF mice. $n = 6$–8 mice for each group. (h) Complementarity between the *miR-23a* seed-matched sequence and the 3′ UTR of NAMPT in *Mus musculus* (Mmu). (i) Luciferase reporter gene assay for interactions between *miR-23a* and its binding site and the mutated binding site in the 3′ UTR of the *Nampt* gene in HEK293T cells. $n = 3$ batches of each group. (j) Representative histograms of the MFI of ROS. (k) Quantification of the MFI of ROS in the three groups. (l) BZBS treatment reversed the *miR-23a* overexpression-induced decrease in GSH levels in primary cultured neurons. (m) The representative original recordings and (n) the analyzed data of mitochondrial oxygen consumption rate (OCR). (o) Comparison of the levels of basal respiration, ATP production, and maximal respiration as assessed by high-resolution respirometry. $n = 4$–6 batches of each group. The data in all the graphs are presented as the mean ± SEM. One-way ANOVA or *t*-test, $^*P < 0.05$ vs the sham or NC group, $^\#P < 0.05$ vs the OXHF or *miR-23a* group, ns: not significant. Omy: oligomycin; FCCP: carbonyl cyanide 4-(trifluoromethoxy)phenylhydrazone; Rot: rotenone; Ama: antimycin A.

Next, we evaluated whether the protective effect of BZBS on OXHF-induced cognitive impairment was due to its inhibition of *miR-23a*. To test this hypothesis, we injected additional AAV-pre-*miR-23a* into the hippocampi of OXHF mice to overcome the inhibitory effect of BZBS on *miR-23a*. We found that AAV-pre-*miR-23a* effectively blocked the protective effects of BZBS on spatial memory (Fig. S12 in Appendix A), episodic memory (Fig. S13 in Appendix A), and nest-building (Fig. S14 in Appendix A) in OXHF mice. In addition, the mitochondria protection exerted by BZBS through the NAMPT–NAD$^+$–SIRT1 and PGC-1α–SIRT3 pathways was blocked by AAV-pre-*miR-23a* injection in OXHF mice (Fig. S15 in Appendix A). Collectively, these results confirmed that BZBS alleviated OXHF-induced cognitive decline by silencing *miR-23a*, thereby reactivating the NAMPT–NAD$^+$–SIRT1 and PGC-1α–SIRT3 mitochondrial antioxidant pathways.

3.4. BZBS regulates miR-23a transcription by targeting AhR

Our study confirmed that BZBS critically regulated mitochondrial antioxidant pathways by suppressing *miR-23a* expression; however, the upstream regulatory mechanism was not clear. BZBS contains 16 ingredients (Table 1) [10], from which 14 unique components were identified by ultra-performance liquid chromatography (UPLC) analysis (Table S5) [37,38]. Multidimensional target

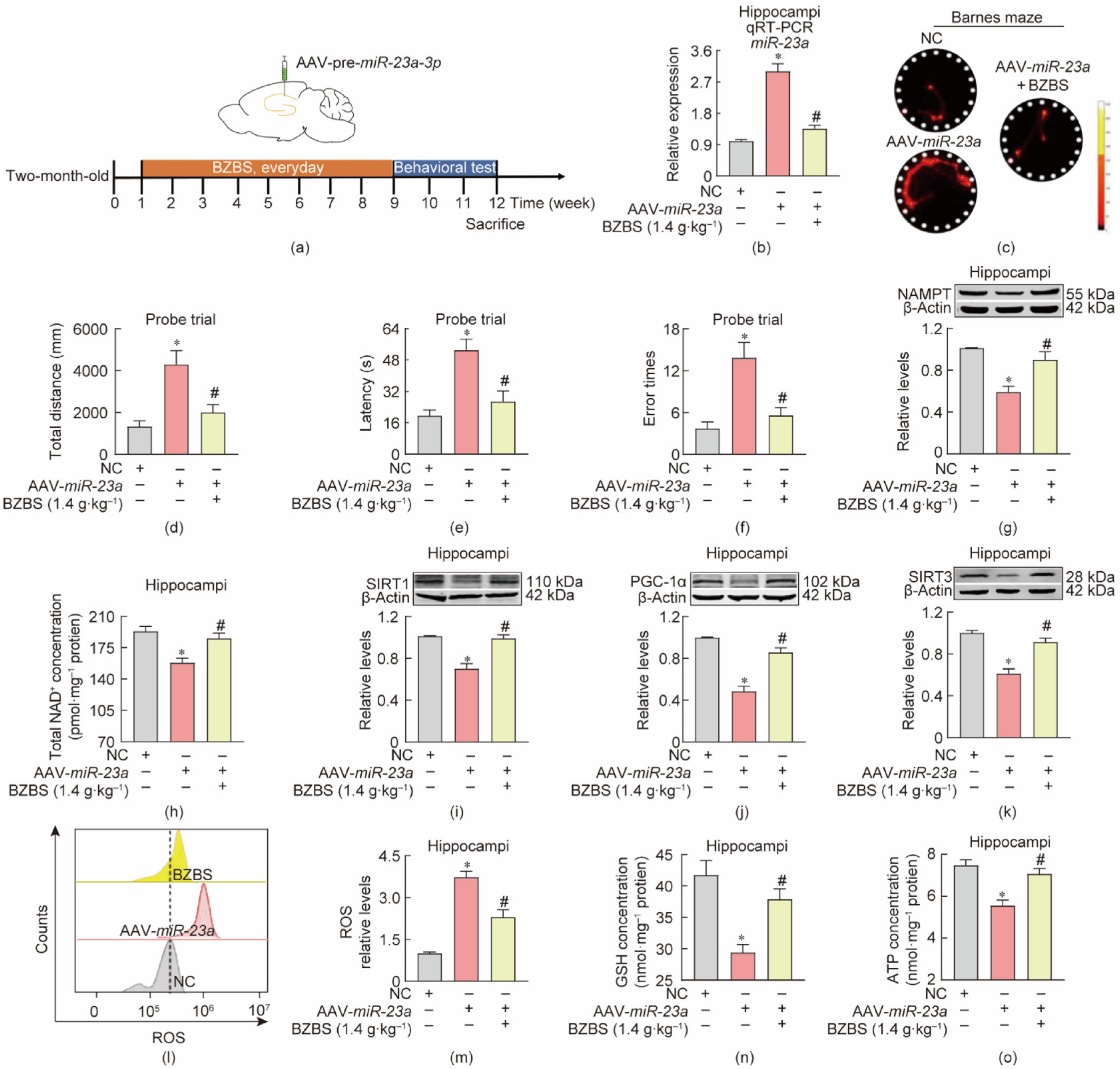

Fig. 4. Effects of BZBS on cognitive function through the *miR-23a*–NAMPT–NAD$^+$–SIRT1 and *miR-23a*–PGC-1α–SIRT3 pathways *in vivo*. (a) Schematic diagram of the experimental timeline. AAV-pre-*miR-23a* was injected into the bilateral hippocampal CA1 region of adult female mice, and the mice were allowed to recover for one week. The mice were treated with BZBS via intragastric injection every day for eight weeks. (b) The expression of *miR-23a* in each group. (c) Representative path tracings from heatmap analysis of the Barnes maze test. (d) Total distance, (e) latency, and (f) error times to reach the target hole in the probe test. (g) Hippocampal NAMPT, (h) total NAD$^+$, and (i) SIRT1 level in each group. (j, k) The levels of hippocampal (j) PGC-1α and (k) SIRT3 in each group. (l) Representative histograms of the MFI and (m) quantification of the MFI of ROS. (n, o) The levels of hippocampal (n) GSH and (o) ATP in all groups. *n* = 6–7 mice for each group. The data in all the graphs are presented as the mean ± SEM. One-way ANOVA, $^*P < 0.05$ vs the NC group, $^\#P < 0.05$ vs the AAV-*miR-23a* group.

prediction using the STP and KEGG databases revealed that the potential targets of 11 of the 14 components were significantly associated with AD pathogenesis (Fig. 5(a)). Further analysis using the TCMSP database identified that six of these, CGA, OST, Sch A, Sch B, HYP, and IMP, had targets related to AD pathways (Fig. 5(b) and (c)). Notably, GO enrichment analysis revealed that the target genes of these six components were significantly clustered in oxidative stress response pathways (Fig. 5(d)), suggesting that these may mediate the antioxidant effects of BZBS.

To determine the specific BZBS components that regulate *miR-23a* expression, we systematically evaluated *miR-23a* levels in SH-SY5Y cells after treatment with the six candidate compounds. After 48 h of treatment, CGA (12 and 24 μmol·L^{-1}), OST (40 μmol·L^{-1}), Sch A (20 and 40 μmol·L^{-1}), and Sch B (4 and 8 μmol·L^{-1}) significantly reduced *miR-23a* expression compared with the solvent (DMSO) (Figs. 5(e)–(h)), whereas HYP and IMP had no effect (Fig. S16 in Appendix A). Building on these findings, we conducted a multidimensional analysis of the four active components (CGA, OST, Sch A, and Sch B) using the STP database, which identified 290 potential molecular targets, nine of which were transcription factors (Fig. 5(i)). To further explore the transcriptional regulatory mechanisms of these four components, we used

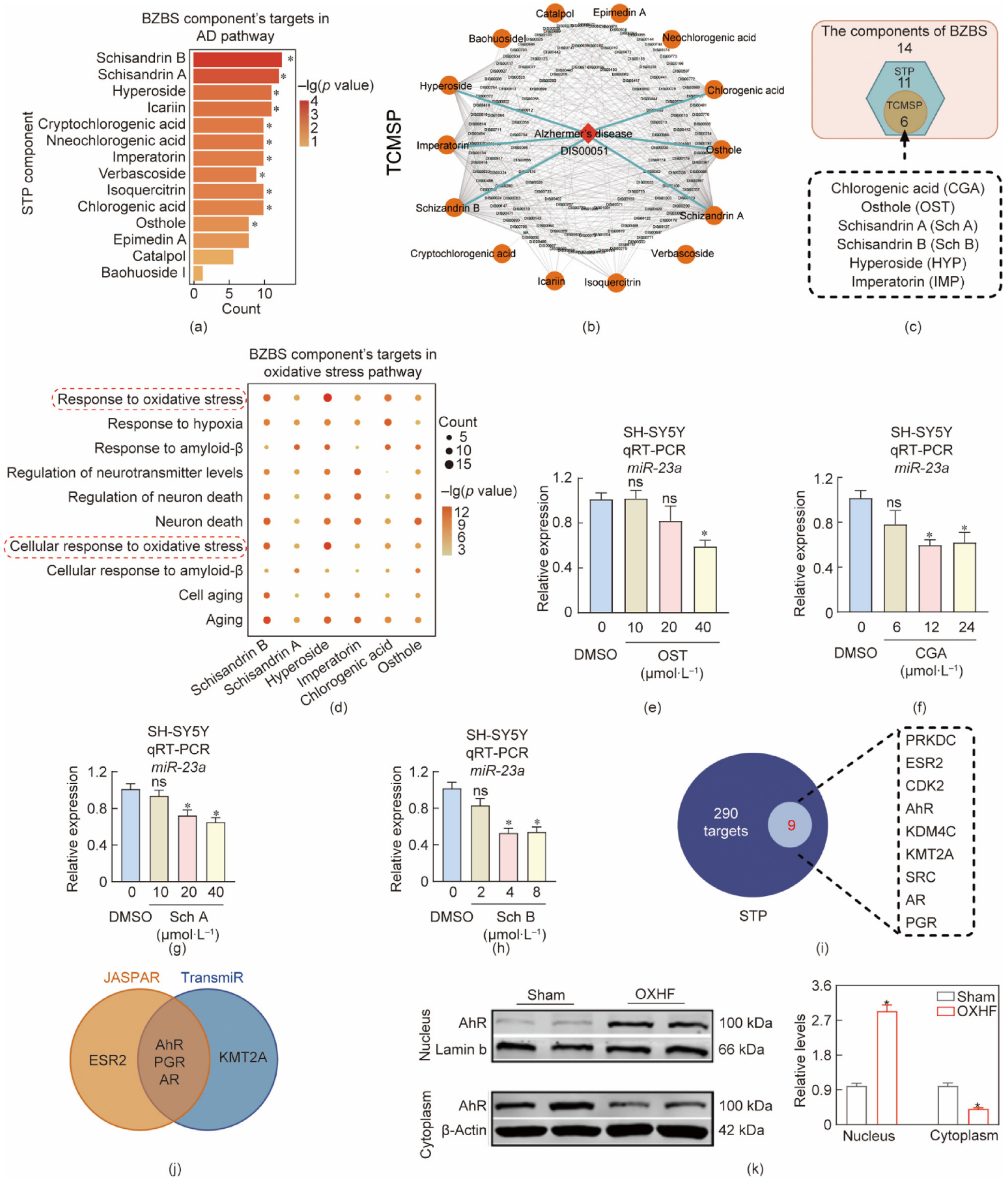

Fig. 5. BZBS is an inhibitor of AhR–*miR-23a* signaling. (a) KEGG enrichment analysis of the targets of the 12 components in BZBS predicted by the STP database. (b) Predicted linking networks between the molecular targets of BZBS components and their related diseases analyzed via the TCMSP database. (c) Overlapping AD-related components are predicted by the STP and TCMSP databases. (d) GO analysis of potential target genes of CGA, OST, Sch A, Sch B, Hyp, and IMP related to AD. (e) OST (40 μmol·L^{-1}) decreases the *miR-23a* expression in SH-SY5Y cells. (f) CGA (12 and 24 μmol·L^{-1}) reduces *miR-23a* levels in SH-SY5Y cells. (g) Sch A (20 and 40 μmol·L^{-1}) decreased the *miR-23a* expression in SH-SY5Y cells. (h) Sch B (4 and 8 μmol·L^{-1}) reduces the *miR-23a* expression in SH-SY5Y cells. $n = 4$ batches of each group. (i) The STP database shows 290 targets of six AD-related compounds of BZBS, nine of which are transcription factors. (j) Venn diagram showing that AhR, PGR, and AR may regulate the expression of *miR-23a*. (k) The levels of the nuclear and cytoplasmic proteins of AhR in each group. $n = 6$ mice for each group. The data in all the graphs are presented as the mean ± SEM. One-way ANOVA or *t*-test, $^*P < 0.05$ vs the DMSO or sham group, ns: not significant.

the JASPAR and TransmiR databases to comprehensively predict transcription factor binding sites. We ultimately identified three candidate transcription factors that could bind the *miR-23a* promoter: AhR, progesterone receptor (PGR), and androgen receptor (AR) (Fig. 5(j)). Western blotting revealed marked nuclear accumulation of the AhR protein in the hippocampi of OXHF model mice

(Fig. 5(k)), while the subcellular distribution of PGR and AR was unchanged (Fig. S17 in Appendix A). Notably, plasma AhR levels also significantly increased in overweight and obese post-menopausal women and were inversely correlated with MoCA scores (Fig. S18 in Appendix A), providing human evidence supporting the pathological relevance of AhR signaling.

To validate the direct targeting effect of BZBS on AhR, molecular docking analysis was conducted to examine the binding capacity between AhR and the BZBS active components (CGA, OST, Sch A, and Sch B). As shown in Figs. 6(a)–(d)), CGA bound to the ligand-binding domain (LBD) of AhR at key residues, including ARG236, ASN121, GLN234, and GLU211, with a binding energy of −5.31 kcal•mol^{-1}. OST also interacted with the LBD by forming hydrogen bonds with GLU211, GLN234, and ARG236, with a binding energy of −7.22 kcal•mol^{-1}. Sch A was predicted to bind at the interface of the LBD and DNA-binding domain (DBD), through hydrophobic interactions with GLN118, THR264, and GLN234 and a binding energy of −8.06 kcal•mol^{-1}. Sch B bound specifically to an allosteric regulatory site adjacent to the LBD through hydrogen bonds with ARG212, GLY235, and GLU211, with a binding energy of −6.75 kcal•mol^{-1}. Collectively, these docking results suggest that all four active components may interact with AhR, thus providing a structural basis for the regulation of AhR by BZBS.

To further assess these interactions under physiological conditions, CETSA was performed. Compared with the DMSO control, BZBS significantly increased the thermal stability of AhR over a broad temperature range (41–53 °C) (Fig. 6(e)). Furthermore, CGA, OST, and Sch B significantly stabilized AhR at 45 and 49 °C, while Sch A stabilized AhR at 45, 49, and 53 °C (Fig. S19 in Appendix A). These results indicated that these four active constituents of BZBS each engaged with AhR in cells, providing qualitative support for constituent-level AhR targeting.

Our previous work confirmed that the transcription factor AhR directly bound to the *miR-23a* promoter in primary neurons [13]; however, *in vivo* evidence to support this has been lacking. In the present study, we performed ChIP analysis, which demonstrated that AhR bound to the −1963 to −995 bp interval of the *miR-23a* promoter in hippocampal tissue (Figs. 6(f)–(j)), consistent with our earlier *in vitro* findings [13]. Therefore, we further examined the dynamic changes in the binding of AhR to the *miR-23a* promoter under pathological conditions. Binding of AhR to the *miR-23a* promoter region was significantly greater in the OXHF group

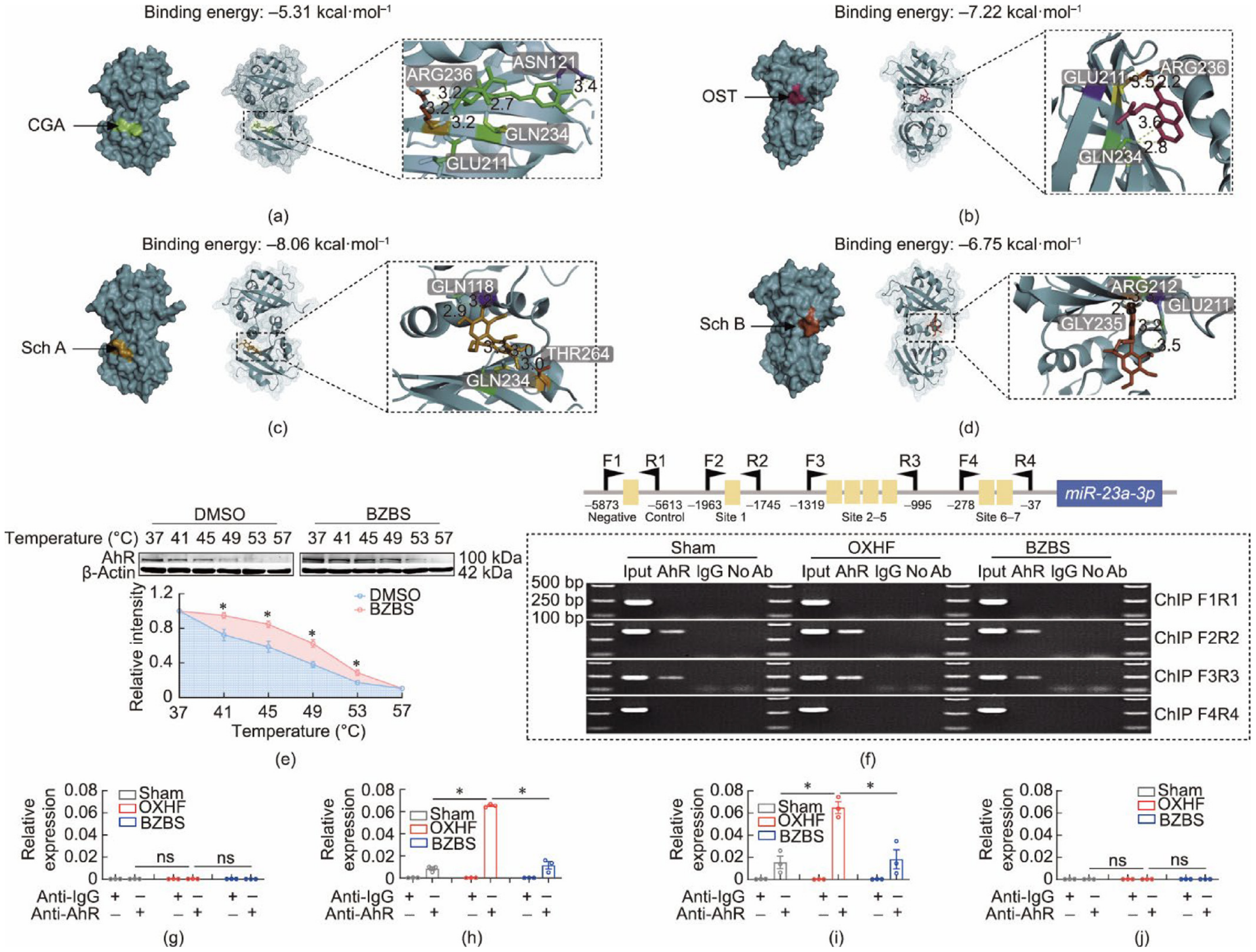

Fig. 6. BZBS targets AhR to regulate the expression of *miR-23a*. (a–d) Docking structures of (a) CGA, (b) OST, (c) Sch A, and (d) Sch B complexed with the AhR protein. (e) The thermal stability of the AhR–BZBS interaction was assessed via CETSA. $n = 6$ batches of each group. (f) The upper panel depicts a schematic diagram of the upstream regulatory region of the mouse *miR-23a* gene, where the conserved potential target binding sites of the AhR are marked with boxes. The bottom panel shows the results of ChIP assays investigating the binding of AhR to the *miR-23a* promoter region (−5873 to −37 bp). AhR binding to these target sites increases *miR-23a* promoter activity. (g–j) qRT-PCR analysis of the AhR binding sequences: (g) ChIP 1, (h) ChIP 2, (i) ChIP 3, (j) ChIP 4. $n = 3$ mice for each group. The data in all the graphs are presented as the mean ± SEM. One-way ANOVA or *t*-test, $^*P < 0.05$, ns: not significant. Iput: input; No Ab: no antibody; IgG: immunoglobulin G.

than in the sham group (Figs. 6(h)–(i)). Notably, BZBS treatment reversed this OXHF-induced increased binding (Figs. 6(h)–(i)), indicating that BZBS effectively modulated AhR and *miR-23a* promoter interactions. Taken together, these *in vivo* findings clearly demonstrated that BZBS regulates *miR-23a* transcription by attenuating AhR activation.

3.5. BZBS alleviates oxidative damage and cognitive decline by inhibiting AhR nuclear translocation

Activated AhR translocates to the nucleus, a process required for its transcriptional regulatory activity [39]. To determine whether AhR nuclear translocation was required for *miR-23a* upregulation and for BZBS to exert its therapeutic effects, we generated AhR constructs with either an intact nuclear localization signal (AhR-nNLS-Flag) or a mutated nuclear localization signal (AhR-mNLS-Flag), as previously reported, to prevent ligand-dependent nuclear localization of AhR [40]. The Flag tag was used to distinguish between exogenous and endogenous AhR. Western blot analysis demonstrated that both Flag-tagged constructs produced high levels of total AhR in primary hippocampal neurons (Fig. 7(a), upper panel). AhR-nNLS-Flag was detected in both the nucleus (middle panel) and the cytoplasm (lower panel); in contrast, AhR-mNLS-Flag was detected exclusively in the cytoplasm (Fig. 7(a)). Following stimulation with the AhR agonist Kyn [11], AhR-nNLS-Flag efficiently translocated to the nucleus, while AhR-mNLS-Flag remained in the cytoplasm (Fig. 7(a)). qRT-PCR analysis showed that, in the absence of Kyn, transfection with either construct alone did not alter *miR-23a* expression. However, upon Kyn stimulation, neurons transfected with AhR-nNLS-Flag showed significantly increased *miR-23a* expression compared with controls transfected with the empty vector. Transfection with AhR-mNLS-Flag did not enhance Kyn-induced *miR-23a* expression (Fig. 7(b)). These findings indicated that Kyn-induced *miR-23a* upregulation required AhR nuclear translocation.

To validate these findings *in vivo*, OXHF mice received bilateral hippocampal injections of AAV-AhR-nNLS or AAV-AhR-mNLS followed by BZBS treatment for eight weeks. Western blot analysis showed that both AAV-AhR-nNLS and AAV-AhR-mNLS injections reversed the BZBS-induced reduction in total AhR protein levels (Figs. 7(c) and (d)). Specifically, AAV-AhR-mNLS produced cytoplasm-limited AhR, whereas AAV-AhR-nNLS underwent normal nuclear translocation (Figs. 7(c) and (d)). qRT-PCR analysis showed that AAV-AhR-nNLS abolished the BZBS-mediated inhibi-

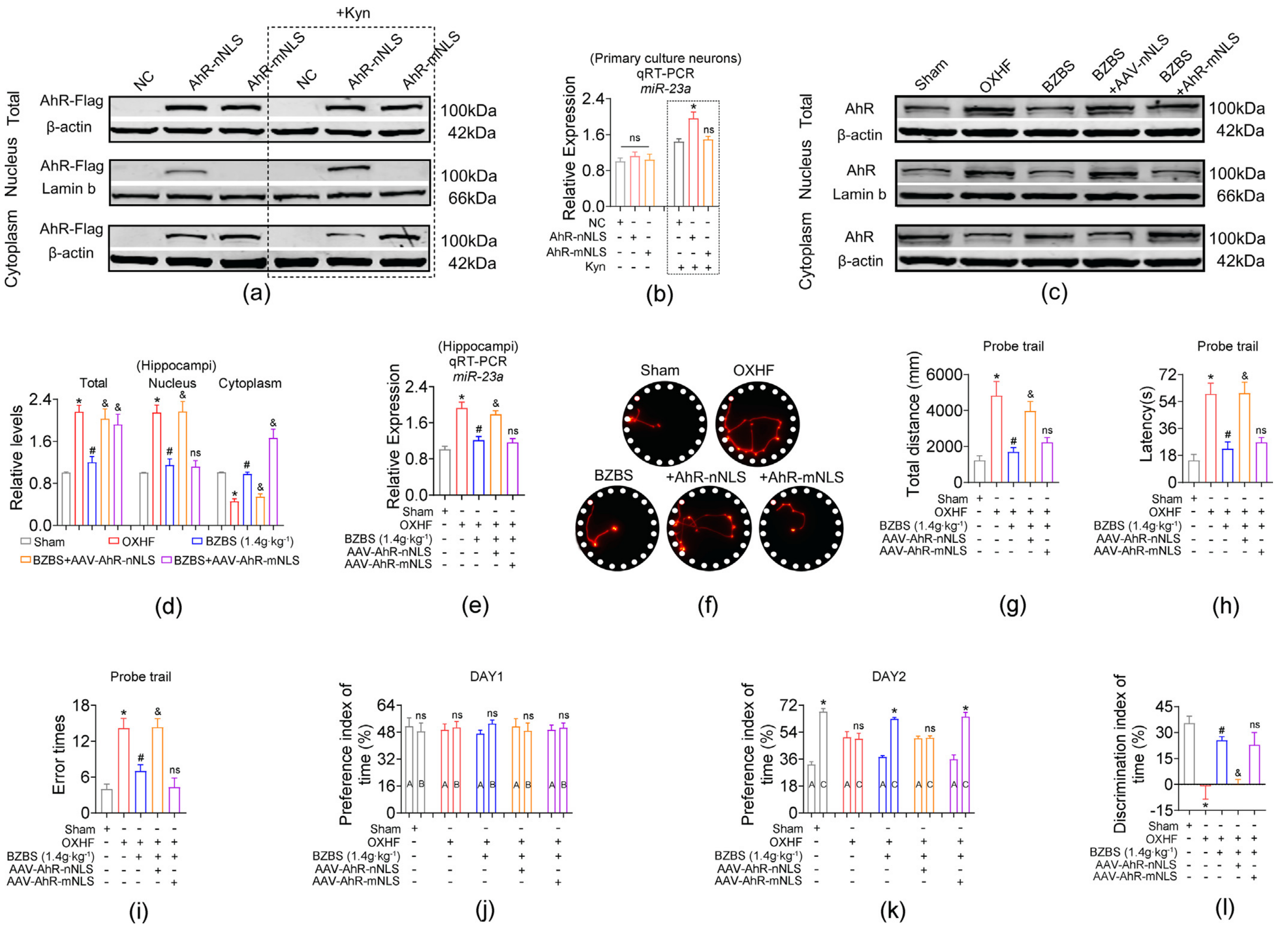

Fig. 7. BZBS-mediated suppression of *miR-23a* depends on AhR nuclear translocation. (a) AhR-Flag protein levels in the cytoplasmic and nuclear fractions of primary hippocampal neurons transfected with AhR-Flag overexpression plasmids. (b) Effect of AhR-nNLS overexpression on *miR-23a* expression in primary hippocampal neurons following Kyn stimulation. $n = 3$ batches per group. (c) Representative Western blot bands and (d) quantification of AhR protein levels in total, nuclear, and cytoplasmic fractions. (e) Hippocampal *miR-23a* expression in each group of mice. (f) Representative search strategy heatmaps from the Barnes maze test. (g) Total distance traveled, (h) latency to the target hole, and (i) number of errors in the Barnes maze probe test. (j) Exploration time of the familiar objects (A and B) in the NOR test on day 1. (k) Preference index for the familiar object (A) and the novel object (C) in the NOR test on day 2. (l) Discrimination index in the NOR test on day 2. $n = 5$–6 mice per group. All data are presented as mean ± SEM. One-way ANOVA or *t*-test, $^*P < 0.05$ vs the NC + Kyn or sham group, $^\#P < 0.05$ vs the OXHF group, $^\&P < 0.05$ vs the BZBS group, ns: not significant.

tion of hippocampal *miR-23a* expression, whereas AAV-AhR-mNLS did not (Fig. 7(e)). Consistently, BZBS failed to improve spatial memory and episodic memory in mice injected with AAV-AhR-nNLS yet further ameliorated cognitive deficits in mice injected with AAV-AhR-mNLS (Figs. 7(f)–(l)). Together, these *in vivo* data supported that AhR nuclear translocation was required for both OXHF-induced pathological signaling and the therapeutic actions of BZBS.

Next, to further verify that AhR activity is required for BZBS to exert its protective effects, we performed a pharmacological rescue experiment with Kyn. Immunofluorescence staining and Western blotting showed that BZBS reduced the nuclear accumulation of AhR in the hippocampus of OXHF mice, whereas Kyn co-treatment markedly reversed this effect (Figs. 8(a) and (b)). Functionally, Kyn restored *miR-23a* expression, abolished the BZBS-mediated activation of the NAMPT–NAD$^+$–SIRT1 and PGC-1α–SIRT3 pathways (Figs. 8(c)–(h)), and significantly weakened the antioxidant effects of BZBS in the hippocampus (Figs. 8(i)–(l)). These findings further supported that BZBS exerted its mitochondrial antioxidant protection, at least in part, by suppressing AhR-dependent *miR-23a* transcription.

After establishing that AhR nuclear translocation must be inhibited for BZBS to exert its mitochondrial antioxidant effects, we next asked whether this molecular pathway contributed to higher-order neural network function and cognition. Hippocampal theta oscillations (4–12 Hz) are neurophysiological hallmarks of spatial navigation and memory consolidation [41]. To determine whether AhR–*miR-23a* axis dysregulation was linked to network-level dysfunction, we assessed the theta rhythm integrity in OXHF mice using *in vivo* electrophysiology techniques (Figs. 9(a) and (b)). Power spectral analysis revealed a marked deterioration of theta oscillations in OXHF mice, as indicated by a reduced peak theta power and frequency (Figs. 9(c)–(e)). Notably, BZBS restored these theta parameters to near-baseline levels, whereas Kyn co-administration completely abolished this effect. Consistently, Kyn also reversed the beneficial effects of BZBS on spatial memory (Figs. 9(f)–(i)), episodic memory (Figs. 9(j)–(l)), and executive function (Figs. 9(m) and (n)).

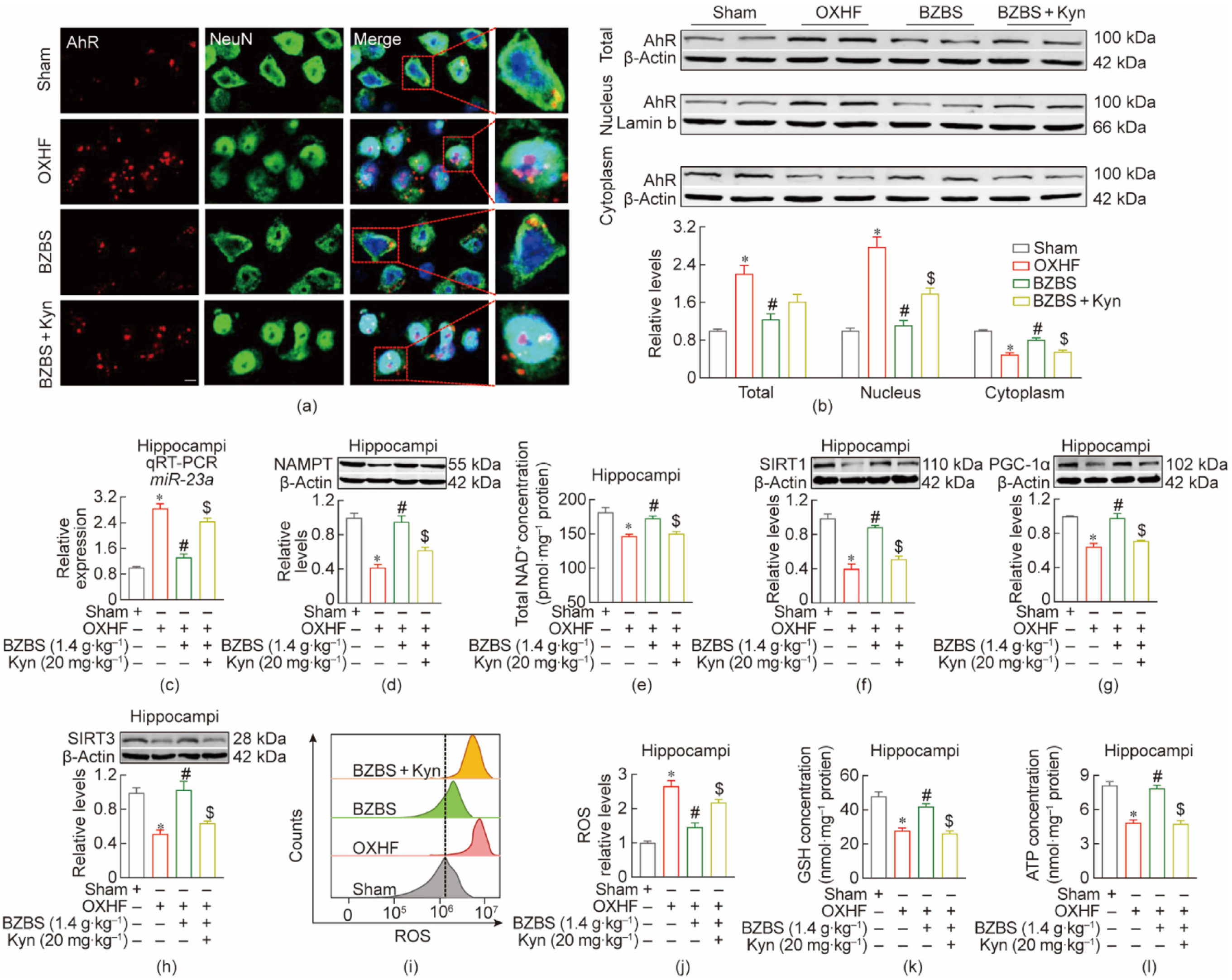

Fig. 8. BZBS reduces *miR-23a*-induced oxidative damage by regulating AhR. (a) Immunofluorescence and (b) Western blotting revealed that Kyn co-treatment reversed the BZBS-induced suppression of nuclear AhR. Scan bar: 20 μm. (c) Kyn triggered *miR-23a* rebound. (d) Hippocampal NAMPT level, (e) total NAD$^+$ content, and (f) SIRT1 level in each group. (g, h) The levels of hippocampal (g) PGC-1α and (h) SIRT3 in each group. (i) Representative histograms of the MFI of ROS in the six groups. (j) Quantification of the MFI of ROS in the six groups. (k, l) The levels of hippocampal (k) GSH and (l) ATP in all groups. $n = 4–6$ mice for each group. The data in all the graphs are presented as the mean ± SEM. One-way ANOVA, $^*P < 0.05$ vs the sham group, $^{\#}P < 0.05$ vs the OXHF group, $^{\$}P < 0.05$ vs the BZBS group.

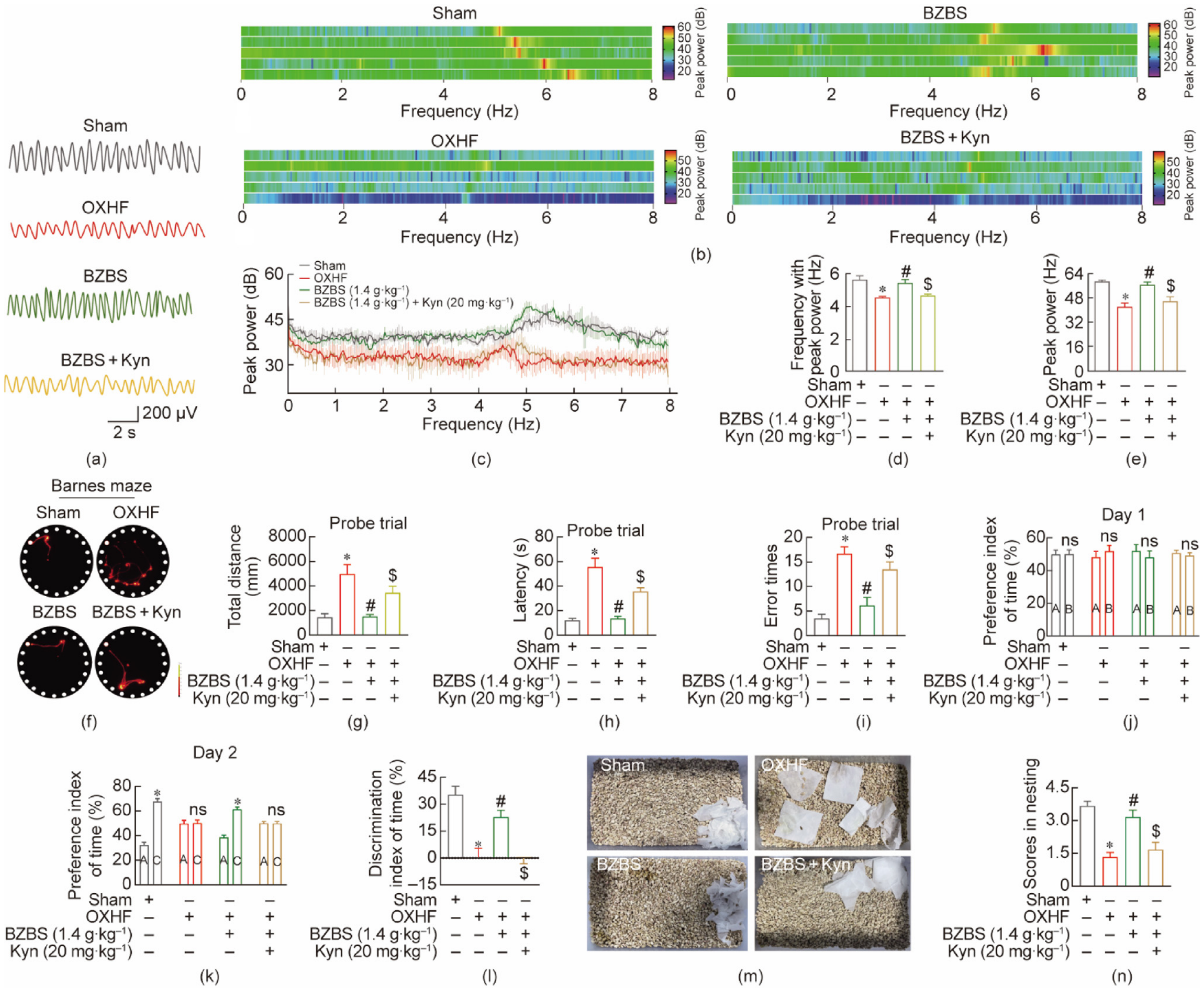

Fig. 9. BZBS rescues theta rhythm synchronization and attenuates cognitive impairment in OXHF mice by inhibiting AhR. (a) Representative LFP waveforms under urethane anesthesia in all groups. (b, c) Heatmaps showing the (b) individual frequency spectrum of the hippocampal LFP frequency spectra and (c) averaged power spectra of hippocampal LFP signals in mice. (d, e) Comparison of the (d) hippocampal theta frequency with peak power and (e) peak power among the above four groups of mice. (f) Representative path tracings from heatmap analysis of the Barnes maze test. (g) Total distance, (h) latency, and (i) error time to reach the target hole in the probe test. (j) There was no difference in the amount of time spent exploring familiar objects (A and B) among the groups on day 1 of the NOR test. (k) The preference indices for objects A and C were calculated on the basis of the exploration time of each group on day 2 of the NOR test. (l) The discrimination index of exploration time in each group on day 2 of the NOR test. (m) Representative images of the nesting test. (n) Nest construction scores of each group. n = 5–6 mice for each group. The data in all the graphs are presented as the mean ± SEM. One-way ANOVA or t-test, $^{*}P < 0.05$ vs the sham group, $^{\#}P < 0.05$ vs the OXHF group, $^{\$}P < 0.05$ vs the BZBS group, ns: not significant.

4. Discussion

Our study is the first to demonstrate that menopausal obesity activates AhR–*miR-23a* crosstalk, dysregulating both the NAMPT–NAD$^+$–SIRT1 and PGC-1α–SIRT3 pathways to drive mitochondrial energy failure, whereas BZBS targets the AhR protein to control *miR-23a*-regulated NAMPT–NAD$^+$–SIRT1 and PGC-1α–SIRT3 pathway activity. This study provides mechanistic validation of the Qi-replenishing bioactivity of BZBS, a novel pathway modulator. The results of this study advance our understanding of the interplay between epigenetic control and neuronal bioenergetics and confirm BZBS as a promising multitarget therapeutic candidate for menopausal obesity-related cognitive impairment.

4.1. Mitochondrial dysfunction as a central pathogenic hub

The OXHF model recapitulates the key features of postmenopausal cognitive impairment, including hippocampal mitochondrial damage, oxidative stress, and bioenergetic failure. Consistent with clinical observations linking mitochondrial dysfunction to neurodegenerative aging [27], OXHF mice had swollen mitochondria with disrupted cristae, reduced ATP production, and increased ROS levels. BZBS treatment ($\geq$ 1.4 g·kg^{-1}) effectively reversed these mitochondrial defects, along with improvements in three behavioral paradigms: spatial memory, assessed by the Barnes maze; episodic memory, evaluated by the NOR test; and executive function and motivational behavior, measured by the nesting test. To benchmark the clinical efficacy of BZBS, we selected DON, a first-line acetylcholinesterase inhibitor, as a positive control in this study. Notably, the behavioral efficacy of BZBS was comparable to that of DON, although their underlying mechanisms appeared to differ. While DON partially rescued SIRT1 (likely by suppressing ROS) [28], BZBS uniquely restored both SIRT1 and SIRT3, suggesting it facilitated broader mitochondrial reprogramming. This finding aligned with emerging evidence that activating both SIRT1 (nuclear NAD$^+$ sensor) and SIRT3 (mitochondrial deacetylase) synergistically enhanced oxidative metabolism and stress resistance [42].

4.2. *miR-23a*: a dual-target epigenetic regulator

A pivotal finding of this study was the identification of *miR-23a* as a master regulator that linked estrogen deficiency to mitochondrial collapse. *miR-23a* overexpression in OXHF hippocampi suppressed both PGC-1α (mitochondrial biogenesis) and NAMPT (NAD^+ salvage), creating a "two-hit" bioenergetic crisis in mitochondria. Mechanistically, *miR-23a* directly targeted the 3′ UTRs of *Ppargc1a* (PGC-1α) and *Nampt*, as confirmed by luciferase assays. BZBS normalized *miR-23a* levels, which reactivated PGC-1α–SIRT3- and NAMPT–NAD^+–SIRT1-mediated redox homeostasis. Importantly, AAV-mediated *miR-23a* overexpression abolished the benefits of BZBS, confirming that the effects of BZBS depended on *miR-23a* silencing. These findings extended prior reports that *miR-23a* functioned in processes from cardiac aging [33] to the central nervous system (CNS), and therefore is a systemic mediator of menopausal metabolic dysfunction. The microRNAs typically regulate multiple targets; our study specifically focused on validating the functional relevance of NAMPT and PGC-1α as key effectors in menopausal obesity. This finding was supported by the consistent rescue of their downstream pathways and mitochondrial phenotypes following BZBS treatment. However, we cannot exclude the possibility that additional *miR-23a* targets may contribute to these phenotypes, which warrants further investigation.

4.3. AhR as a novel target of BZBS

The discovery that AhR is the transcriptional driver of *miR-23a* in OXHF mice is a significant advance. AhR, a ligand-activated transcription factor, accumulates in hippocampal nuclei under estrogen deficiency where it directly binds the *miR-23a* promoter [13]. In this study, by integrating bioinformatics, molecular biology, and neurophysiology, we found that BZBS suppressed AhR aggregation in the nucleus, likely through the bioactive components of BZBS, CGA, OST, Sch A, and Sch B. This hypothesis was strengthened by evidence from a battery of experiments, including molecular docking, CETSA-based target engagement, and *in vivo* ChIP assays on hippocampal tissue. Importantly, Kyn, a physiological activator of AhR, was shown to negatively correlate with serum estrogen levels in women [43–45]. Kyn-mediated activation of AhR induced its pathological nuclear translocation, an essential molecular event mechanistically linked to aggravated obesity-associated metabolic dysfunction and AD pathogenesis [11,46]. In the present study, we found that Kyn reversed the BZBS-induced reduction in nuclear AhR accumulation and abolished BZBS-regulated *miR-23a* expression and levels of its downstream signaling molecules, including SIRT1, PGC-1α, and SIRT3, and the oxidative stress markers ROS, GSH, and ATP. Collectively, these findings provided the first evidence of the AhR–*miR-23a* axis as a potential therapeutic target in menopausal obesity-related cognitive impairment. Genetic manipulation using AhR-nNLS and AhR-mNLS further confirmed that AhR nuclear translocation was required for pathological signaling and represents a critical step forward in understanding the therapeutic mechanism of BZBS, as BZBS exerted its *miR-23a*-suppressive and cognitive-protective effects only when AhR nuclear entry was blocked.

4.4. Multicomponent synergy in BZBS

The pharmacological complexity of BZBS, with 14 identified bioactive compounds, is the basis of its multitarget efficacy. BZBS was formulated according to the theory of the *Yellow Emperor's Canon of Internal Medicine*, a foundational TCM doctrine emphasizing a balance among Qi, blood, Yin, and Yang across the five viscera, with a focus on tonifying Qi and supporting kidney function to counteract aging and chronic diseases. Intriguingly, in TCM, the concept of "Qi deficiency" is considered the root of aging, which aligns with modern medical insights into the effects of low mitochondrial ATP production [14], a hallmark of age-related neurodegenerative and cardiovascular disorders [15]. This similarity between ancient theory and contemporary science was exemplified by the restoration of mitochondrial ATP synthesis mediated by BZBS, mechanistically bridging the TCM concept of "Qi" with bioenergetic regulation. Functional screening revealed that *miR-23a* expression was significantly suppressed *in vitro* by four key BZBS components, CGA, OST, Sch A, and Sch B (but not HYP or IMP), which aligned with their AhR-modulating and antioxidant properties. For example, Sch B was reported to enhance mitochondrial energy metabolism by increasing the protein expression of SIRT3 in H_2O_2-stimulated HT22 cells [47], and CGA was shown to scavenge oxidized low-density lipoprotein (oxLDL)-induced endothelial oxidative damage and mitochondrial dysfunction by increasing SIRT1 expression [48]. These findings suggest that multiple bioactive components of BZBS may collectively contribute to its overall activity, potentially exerting broad pathway regulation rather than targeting a single pathway lacking direct mitochondrial or epigenetic effects. This integration of TCM principles with molecular mechanisms underscores the unique ability of herbal formulations to address the multifactorial pathology of chronic diseases. Therefore, precisely elucidating how individual small molecules within TCM formulations interact to target intracellular molecular pathways is key to advancing the globalization of TCM. By accurately mapping the metabolic characteristics of BZBS after administration and detecting the concentrations of small-molecule compounds that enter the brain, the mechanisms by which BZBS improves cognitive decline in menopausal women with obesity can be further elucidated.

4.5. Translational relevance and limitations

The preclinical findings presented here have several implications for future clinical research. First, we demonstrated that BZBS effectively ameliorated cognitive deficits and mitochondrial dysfunction in OXHF mice by inhibiting the AhR–*miR-23a* axis and activating the NAMPT–NAD^+–SIRT1 and PGC-1α–SIRT3 pathways at doses of 1.4 and 2.8 $g \cdot kg^{-1}$, whereas a 0.7 $g \cdot kg^{-1}$ dose had no significant effects. However, these findings only provide experimental evidence to inform clinical dose selection in individualized administration (e.g., in patients with elevated AhR/*miR-23a* expression). Moreover, the unique dual-pathway regulatory mechanism of BZBS (unlike that of DON, in which only SIRT1 is affected) suggests that BZBS may warrant further investigation in postmenopausal patients with cognitive impairment accompanied by mitochondrial dysfunction. Second, although we believe that BZBS inhibits AhR, the intensity of the inhibitory effect relative to that of BAY-218 (AhR antagonist) should be thoroughly evaluated. Additionally, although the OXHF model effectively recapitulates the interaction between estrogen deficiency and obesity, it does not reflect key features of human AD pathology, including amyloid-β deposition and tau hyperphosphorylation. Future studies using models with classical AD pathology may help determine whether the benefits of BZBS extend beyond menopausal obesity-related cognitive impairment.

In addition to mechanistic insights and disease model considerations, the optimal therapeutic regimen that will translate the preclinical promise of BZBS into clinical practice remains a critical unknown factor. Specifically, whether greater efficacy can be achieved by directly targeting AhR or *miR-23a* than by using the multicomponent BZBS formulation is likely to depend on the clinical context. Although single-target interventions can precisely modulate specific pathways in menopausal obesity, they may fail to address the broader systemic perturbations associated with the disease, such as metabolic dysfunction and neuroinflammation, that are simultaneously targeted by BZBS [49,50].

Although a previous clinical study reported that 12 weeks of BZBS treatment did not produce adverse changes in vital signs, physical examination findings, electrocardiogram results, or laboratory values compared with those at baseline [7], potential long-term and dose-dependent side effects still warrant further evaluation.

Our previous study demonstrated that neither mice undergoing OVX surgery alone nor sham mice fed an HFD exhibited cognitive decline after two months. In contrast, OXHF mice showed significant cognitive impairment [4]. Therefore, in this study, we did not include a non-OVX obese control group. Further study is needed to disentangle the respective contributions of obesity and estrogen deprivation to cognitive decline in patients with menopausal obesity.

Our clinical cohort study showed elevated plasma AhR and *miR-23a* levels in overweight or obese postmenopausal women, and both levels negatively correlated with cognitive function. These findings provide initial clinical support demonstrating the involvement of the AhR–*miR-23a* axis in cognitive impairment in this population. However, the relatively small sample size and the absence of intervention data preclude conclusions on whether BZBS can regulate this axis or improve cognitive function in clinical settings. Future studies with larger cohorts are needed to determine whether AhR and *miR-23a* plasma levels and cognitive performance change dynamically in response to BZBS intervention.

5. Conclusion

BZBS orchestrates cognitive recovery in menopausal obese subjects through a sequential mechanism in which AhR-mediated *miR-23a* transcription is inhibited. The consequent downregulation of *miR-23a* reactivates the PGC-1α–SIRT3 and NAMPT–NAD$^+$–SIRT1 pathways to restore the mitochondrial ATP/ROS balance (Fig. 10). Although previous studies demonstrated the clinical potential of BZBS [38], the present study is the first to translate the TCM concept of "replenishing Qi" mediated by BZBS into a framework of mitochondrial function. Collectively, our findings identified BZBS as a promising therapeutic candidate for menopausal obesity-related cognitive decline. With its preclinical efficacy and established clinical safety profile, BZBS merits further investigation in human studies.

CRediT authorship contribution statement

Xiaobin An: Writing – review & editing, Writing – original draft, Formal analysis, Data curation, Conceptualization. **Wentao Xu:** Writing – review & editing, Writing – original draft, Formal analysis, Data curation, Conceptualization. **Haining Chen:** Methodology, Investigation, Formal analysis, Data curation. **Mingyou**

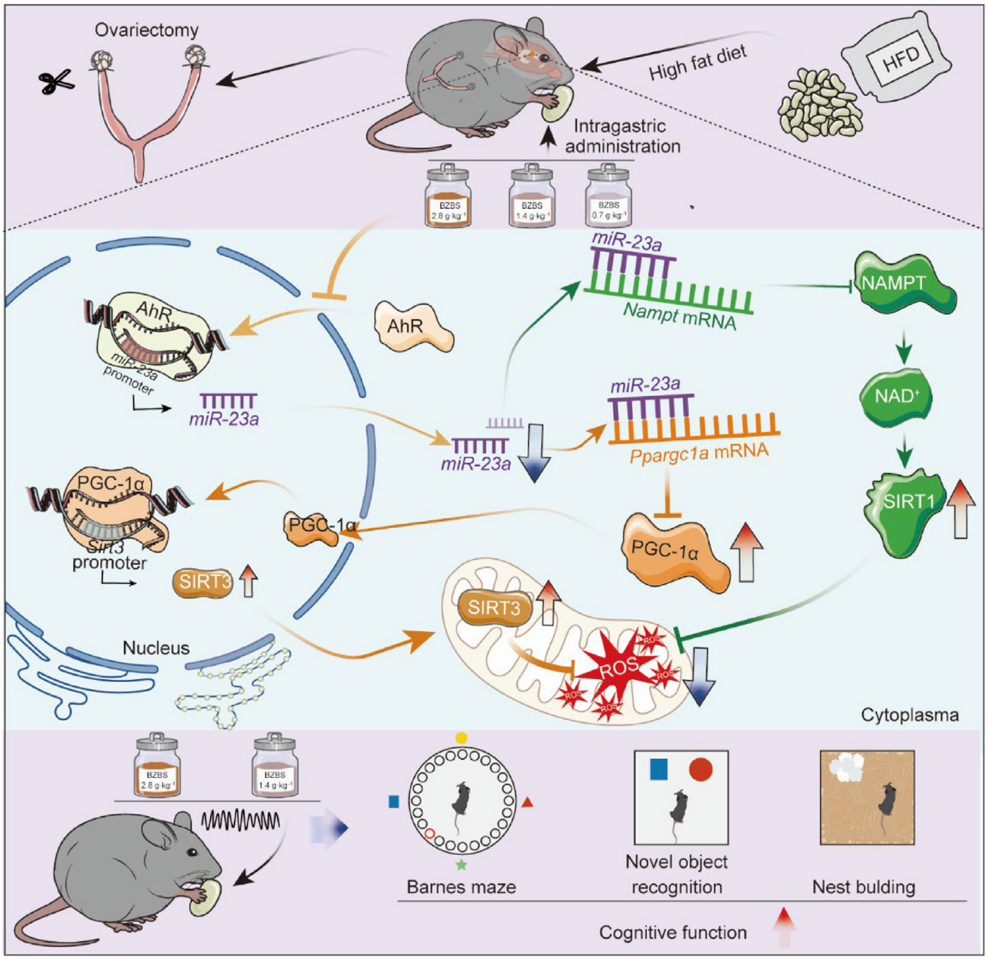

Fig. 10. Mechanism by which BZBS ameliorates cognitive decline in the OXHF mice by protecting against mitochondrial damage.

Zhang: Methodology, Data curation. **Xiaojing Zhong:** Methodology, Investigation. **Jing Liu:** Validation. **Haihui Chen:** Data curation. **Xinyue Zhao:** Data curation. **Yan Wu:** Methodology, Formal analysis, Data curation. **Jing Li:** Writing – review & editing, Supervision, Funding acquisition, Conceptualization. **Jinan Yang:** Validation. **Meijie Chen:** Methodology, Data curation. **Lu Zeng:** Data curation. **Jing Ma:** Data curation. **Xuqiao Wang:** Validation. **Hongrong Li:** Validation. **Yanpeng Xue:** Methodology. **Qin Wang:** Validation. **Dongyang Wang:** Validation. **Guitian Cong:** Methodology, Data curation. **Yunlong Hou:** Funding acquisition, Conceptualization. **Zhenhua Jia:** Funding acquisition, Conceptualization. **Jing Ai:** Writing – review & editing, Supervision, Funding acquisition, Conceptualization.

Declaration of competing interest

The authors declare the following financial interests/personal relationships which may be considered as potential competing interests: Prof. Zhenhua Jia reports affiliated with Hebei Yiling Hospital, a nonprofit medical institution, which is two completely independent legal entities with Shijiazhuang Yiling Pharmaceutical Co., Ltd. Prof Jia is the spouse of Ms. Rui Wu, who holds shares and serves as a director of Shijiazhuang Yiling Pharmaceutical Co., Ltd. He has fully disclosed these interests to the research committee and has developed an approved plan to manage any potential conflicts that may arise from such an arrangement and ensures the scientificity, objectivity, and authority of the research results.

Acknowledgments

This work was supported by the National Key Research and Development Program of China “Modernization of Traditional Chinese Medicine” (2023YFC3504300), the Key Research and Development Program of Heilongjiang Province (GA21C009), the STI2030-Major Projects (2022ZD0211804), the High-level S & T Innovation and Entrepreneurship Talent Project of Shijiazhuang (07202203), and the National Natural Science Foundation of China (82501458).

We thank LetPub for its linguistic assistance during the preparation of this manuscript.

Appendix A. Supplementary data

Supplementary data to this article can be found online at https://doi.org/10.1016/j.eng.2026.05.005.

References

[1] Yan QY, Lv JL, Shen XY, Ou-Yang XN, Yang JZ, Nie RF, et al. Patchouli alcohol as a selective estrogen receptor β agonist ameliorates AD-like pathology of APP/PS1 model mice. Acta Pharmacol Sin 2022;43(9):2226–41.

[2] Cui J, Ait-Ghezala G, Sambamurti K, Gao F, Shen Y, Li R. Sex-specific regulation of β-secretase: a novel estrogen response element (ERE)-dependent mechanism in Alzheimer’s disease. J Neurosci 2022;42(6):1154–65.

[3] Floud S, Simpson RF, Balkwill A, Brown A, Goodill A, Gallacher J, et al. Body mass index, diet, physical inactivity, and the incidence of dementia in 1 million UK women. Neurology 2020;94(2):e123–32.

[4] Zhang S, Zeng L, Ma J, Xu W, Qu Y, Wang X, et al. Gut Prevotellaceae-GABAergic septohippocampal pathway mediates spatial memory impairment in high-fat diet-fed ovariectomized mice. Neurobiol Dis 2023;177:105993.

[5] Pratchayasakul W, Sa-Nguanmoo P, Sivasinprasasn S, Pintana H, Tawinvisan R, Sripetchwandee J, et al. Obesity accelerates cognitive decline by aggravating mitochondrial dysfunction, insulin resistance and synaptic dysfunction under estrogen-deprived conditions. Horm Behav 2015;72:68–77.

[6] Hruby A, Hu FB. The epidemiology of obesity: a big picture. PharmacoEconomics 2015;33(7):673–89.

[7] Mei J, Ju C, Wang B, Gao R, Zhang Y, Zhou S, et al. The efficacy and safety of Bazi Bushen capsule in treating premature aging: a randomized, double blind, multicenter, placebo-controlled clinical trial. Phytomedicine 2024;130:155742.

[8] Li L, Chen B, An T, Zhang H, Xia B, Li R, et al. BaZiBuShen alleviates altered testicular morphology and spermatogenesis and modulates Sirt6/P53 and Sirt6/NF-κB pathways in aging mice induced by *D*-galactose and NaNO$_2$. J Ethnopharmacol 2021;271:113810.

[9] Li L, Zhang H, Chen B, Xia B, Zhu R, Liu Y, et al. BaZiBuShen alleviates cognitive deficits and regulates Sirt6/NRF2/HO-1 and Sirt6/P53-PGC-1α-TERT signaling pathways in aging mice. J Ethnopharmacol 2022;282:114653.

[10] Huang D, Wang X, Zhu Y, Gong J, Liang J, Song Y, et al. Bazi Bushen capsule alleviates post-menopausal atherosclerosis via GPER1-dependent anti-inflammatory and anti-apoptotic effects. Front Pharmacol 2021;12:658998.

[11] Huang T, Song J, Gao J, Cheng J, Xie H, Zhang L, et al. Adipocyte-derived kynurenine promotes obesity and insulin resistance by activating the AhR/STAT3/IL-6 signaling. Nat Commun 2022;13(1):3489.

[12] Kretzschmar G, Papke A, Zierau O, Möller FJ, Medjakovic S, Jungbauer A, et al. Estradiol regulates aryl hydrocarbon receptor expression in the rat uterus. Mol Cell Endocrinol 2010;321(2):253–7.

[13] Zhang S, An X, Huang S, Zeng L, Xu Y, Su D, et al. AhR/miR-23a-3p/PKCα axis contributes to memory deficits in ovariectomized and normal aging female mice. Mol Ther Nucleic Acids 2021;24:79–91.

[14] Gao RY, Gao JR, Zhao HY, Lan T, Tseng YD. Mechanism of tonifying Qi by traditional Chinese medicine from mitochondrial dynamics. Zhongguo Zhong Yao Za Zhi 2023;48(13):3684–92. Chinese.

[15] Amorim JA, Coppotelli G, Rolo AP, Palmeira CM, Ross JM, Sinclair DA. Mitochondrial and metabolic dysfunction in ageing and age-related diseases. Nat Rev Endocrinol 2022;18(4):243–58.

[16] Koizumi M, Tatebe J, Watanabe I, Yamazaki J, Ikeda T, Morita T. Aryl hydrocarbon receptor mediates indoxyl sulfate-induced cellular senescence in human umbilical vein endothelial cells. J Atheroscler Thromb 2014;21(9):904–16.

[17] He J, Hu B, Shi X, Weidert ER, Lu P, Xu M, et al. Activation of the aryl hydrocarbon receptor sensitizes mice to nonalcoholic steatohepatitis by deactivating mitochondrial sirtuin deacetylase Sirt3. Mol Cell Biol 2013;33(10):2047–55.

[18] An X, Xu W, Zhao X, Chen H, Yang J, Wu Y, et al. Bazi Bushen capsule attenuates cardiac systolic injury via SIRT3/SOD2 pathway in high-fat diet-fed ovariectomized mice. Heliyon 2024;10(11):e32159.

[19] Zhou Y, Zhu F, Liu Y, Zheng M, Wang Y, Zhang D, et al. Blood–brain barrier-penetrating siRNA nanomedicine for Alzheimer’s disease therapy. Sci Adv 2020;6(41):eabc7031.

[20] Wang N, Sun LY, Zhang SC, Wei R, Xie F, Liu J, et al. MicroRNA-23a participates in estrogen deficiency induced gap junction remodeling of rats by targeting GJA1. Int J Biol Sci 2015;11(4):390–403.

[21] Ai J, Sun LH, Che H, Zhang R, Zhang TZ, Wu WC, et al. MicroRNA-195 protects against dementia induced by chronic brain hypoperfusion via its anti-amyloidogenic effect in rats. J Neurosci 2013;33(9):3989–4001.

[22] Li F, Jiang M, Ma M, Chen X, Zhang Y, Zhang Y, et al. Anthelmintics nitazoxanide protects against experimental hyperlipidemia and hepatic steatosis in hamsters and mice. Acta Pharm Sin B 2022;12(3):1322–38.

[23] Daina A, Michielin O, Zoete V. SwissTargetPrediction: updated data and new features for efficient prediction of protein targets of small molecules. Nucleic Acids Res 2019;47(W1):W357–64.

[24] Ru J, Li P, Wang J, Zhou W, Li B, Huang C, et al. TCMSP: a database of systems pharmacology for drug discovery from herbal medicines. J Cheminform 2014;6(1):13.

[25] Chen M, Zhong G, Liu M, He H, Zhou J, Chen J, et al. Integrating network analysis and experimental validation to reveal the mitophagy-associated mechanism of Yiqi Huoxue (YQHX) prescription in the treatment of myocardial ischemia/reperfusion injury. Pharmacol Res 2023;189:106682.

[26] Chen YM, Xu W, Liu Y, Zhang JH, Yang YY, Wang ZW, et al. Anomanolide C suppresses tumor progression and metastasis by ubiquitinating GPX4-driven autophagy-dependent ferroptosis in triple negative breast cancer. Int J Biol Sci 2023;19(8):2531–50.

[27] Stefanatos R, Sanz A. The role of mitochondrial ROS in the aging brain. FEBS Lett 2018;592(5):743–58.

[28] Jian WX, Zhang Z, Zhan JH, Chu SF, Peng Y, Zhao M, et al. Donepezil attenuates vascular dementia in rats through increasing BDNF induced by reducing HDAC6 nuclear translocation. Acta Pharmacol Sin 2020;41(5):588–98.

[29] Covarrubias AJ, Perrone R, Grozio A, Verdin E. NAD$^+$ metabolism and its roles in cellular processes during ageing. Nat Rev Mol Cell Biol 2021;22(2):119–41.

[30] Wang D, Cao L, Zhou X, Wang G, Ma Y, Hao X, et al. Mitigation of honokiol on fluoride-induced mitochondrial oxidative stress, mitochondrial dysfunction, and cognitive deficits through activating AMPK/PGC-1α/Sirt3. J Hazard Mater 2022;437:129381.

[31] Devarakonda S, Gupta K, Chalmers MJ, Hunt JF, Griffin PR, Van Duyne GD, et al. Disorder-to-order transition underlies the structural basis for the assembly of a transcriptionally active PGC-1α/ERRγ complex. Proc Natl Acad Sci USA 2011;108(46):18678–83.

[32] Ventura-Clapier R, Garnier A, Veksler V. Transcriptional control of mitochondrial biogenesis: the central role of PGC-1alpha. Cardiovasc Res 2008;79(2):208–17.

[33] Sun LY, Wang N, Ban T, Sun YH, Han Y, Sun LL, et al. MicroRNA-23a mediates mitochondrial compromise in estrogen deficiency-induced concentric remodeling via targeting PGC-1α. J Mol Cell Cardiol 2014;75:1–11.

[34] Zhang J, Xiang H, Liu J, Chen Y, He RR, Liu B. Mitochondrial sirtuin 3: new emerging biological function and therapeutic target. Theranostics 2020;10(18):8315–42.

[35] Zhao Y, Zhang J, Zheng Y, Zhang Y, Zhang XJ, Wang H, et al. NAD^+ improves cognitive function and reduces neuroinflammation by ameliorating mitochondrial damage and decreasing ROS production in chronic cerebral hypoperfusion models through Sirt1/PGC-1α pathway. J Neuroinflammation 2021;18(1):207.

[36] Lautrup S, Sinclair DA, Mattson MP, Fang EF. NAD^+ in brain aging and neurodegenerative disorders. Cell Metab 2019;30(4):630–55.

[37] Huang D, Hu H, Chang L, Liu S, Liang J, Song Y, et al. Chinese medicine Bazi Bushen capsule improves lipid metabolism in ovariectomized female $ApoE^{-/-}$ mice. Ann Palliat Med 2020;9(3):1073–83.

[38] Ji C, Wei C, Li M, Shen S, Zhang S, Hou Y, et al. Bazi Bushen capsule attenuates cognitive deficits by inhibiting microglia activation and cellular senescence. Pharm Biol 2022;60(1):2025–39.

[39] Yang CE, Wang YN, Hua MR, Miao H, Zhao YY, Cao G. Aryl hydrocarbon receptor: from pathogenesis to therapeutic targets in aging-related tissue fibrosis. Ageing Res Rev 2022;79:101662.

[40] Cui L, Wang Z, Guo Z, Zhang H, Liu Y, Zhang H, et al. Tryptophan metabolite indole-3-aldehyde induces AhR and c-MYC degradation to promote tumor immunogenicity. Adv Sci 2025;12(36):e09533.

[41] Herweg NA, Solomon EA, Kahana MJ. Theta oscillations in human memory. Trends Cogn Sci 2020;24(3):208–27.

[42] Gu T, Liu J, Zeng T, Chen L, Tian Y, Xu W, et al. New insights into ovarian regression-related mitochondrial dysfunction in the late-laying period. Poult Sci 2025;104(4):104938.

[43] Sha Q, Achtyes E, Nagalla M, Keaton S, Smart L, Leach R, et al. Associations between estrogen and progesterone, the kynurenine pathway, and inflammation in the post-partum. J Affect Disord 2021;281:9–12.

[44] de Bie J, Guest J, Guillemin GJ, Grant R. Central kynurenine pathway shift with age in women. J Neurochem 2016;136(5):995–1003.

[45] Liu J, Si J, Zhao W. Investigation of the effect of Tai Chi training on depressive symptoms in perimenopausal women on the basis of serum kynurenine metabolites. Exp Aging Res 2025;51(3):331–49.

[46] Duan Z, Zhang S, Liang H, Xing Z, Guo L, Shi L, et al. Amyloid β neurotoxicity is IDO1–Kyn–AhR dependent and blocked by IDO1 inhibitor. Signal Transduct Target Ther 2020;5(1):96.

[47] Hu F, Tong S, Xu H, Schisandrin B. Schisandrin B improves mitochondrial function and inhibits HT22 cell apoptosis by regulating Sirt3 protein. J Membr Biol 2025;258(2):123–33.

[48] Tsai KL, Hung CH, Chan SH, Hsieh PL, Ou HC, Cheng YH, et al. Chlorogenic acid protects against oxLDL-induced oxidative damage and mitochondrial dysfunction by modulating Sirt1 in endothelial cells. Mol Nutr Food Res 2018;62(11):e1700928.

[49] Shen X, Li M, Li Y, Jiang Y, Niu K, Zhang S, et al. Bazi Bushen ameliorates age-related energy metabolism dysregulation by targeting the IL-17/TNF inflammatory pathway associated with SASP. Chin Med 2024;19(1):61.

[50] Huang H, Lu W, Huang Y, Su Y, Luo R, Zeng Y, et al. Bazi Bushen improves cognitive dysfunction in 5× FAD mice by targeting amyloid pathology, neuroinflammation and cellular senescence. J Ethnopharmacol 2025;355(Pt A):120586.